Natural Microbial Enrichment Modulates Microglial States and Transcriptional Programs Relevant to Alzheimer's Disease

Amir Mohamed Kezai [1,2 #], Mohamed Lala Bouali [1,2 #], Marc Bazin [1], Papa Yaya Badiane [1], Nasim Eskandari [4,5], Véronique Lévesque [1,2], Justin Robillard [6], Denis Soulet [1,3], Cyntia Tremblay [1], Frédéric Calon [1,3], Françoise Morin [1], Luc Vallières [1,4], Sébastien S. Hébert [1,2 *]

[1] Centre de recherche du CHU de Québec - Université Laval, Axe neurosciences, Québec, Canada

[2] Université Laval, Département de psychiatrie et de neurosciences, Québec, Canada

[3] Université Laval, Département de pharmacie, Québec, Canada

[4] Université Laval, Département de microbiologie-infectiologie et d'immunologie, Québec, Canada

[5] Université Laval, Département de biologie moléculaire, biochimie médicale et pathologie, Québec, Canada

[6] Centre de recherche Institut universitaire de cardiologie et de pneumologie de Québec, Québec, Canada

# These authors contributed equally to this work.

Corresponding author:

Dr. Sébastien S. Hébert
CHU de Québec Research Center, CHUL
2705 Laurier Boul.
Neurosciences Unit, Room R3-704.5
Québec (Québec) G1V 4G2
Canada
Phone : (418) 525-4444 ext. 49233
Email: sebastien.hebert@crchudequebec.ulaval.ca

Keywords : Rewilding, microglia, neuroinflammation, immunity, brain, Alzheimer's disease, 5xFAD

ABSTRACT

The diversity of environmental microbial exposure is a key driver of immune maturation and host defense; however, its impact on brain immunity and neurodegenerative diseases remains poorly documented. Here, we show that controlled indoor rewilding, by introducing a natural farm-like environment into laboratory housing, reshapes peripheral and central nervous system (CNS) immune networks in wild-type (WT) and 5xFAD mice, a model of Alzheimer's disease (AD). Compared with traditional specific pathogen-free (SPF) housing, rewilded mice exhibited systemic shifts toward mature immune phenotypes, including increases in effector and memory B and T cells, expansion of plasma cell populations, and alterations in immunoglobulin isotypes. In the brain, indoor rewilding recalibrated microglial and astrocytic activation of SPF-5xFAD mice, attenuating pro-inflammatory transcriptional programs while enhancing homeostatic, complement, and phagocytic signatures. A strong transcriptional convergence was observed between rewilded and wild mice, with rewilded 5xFAD mice exhibiting greater similarity to human AD transcriptional profiles. Morphological and histochemical analyses confirmed that rewilded microglia adopt metabolically adaptable, homeostatic states that influence amyloid-β plaque binding and clearance. Collectively, these findings suggest that microbial diversity through "dirty" mouse modeling could enhance the translational relevance of neuroimmunology and neurodegenerative disease research.

INTRODUCTION

The peripheral and CNS immune systems interact in a continuous and bidirectional manner to orchestrate host defense, maintain tissue homeostasis, and resolve inflammation[1–3]. Microglia, the primary resident immune cells of the brain, integrate signals from neurons, astrocytes, endothelial cells, and perivascular macrophages, while remaining responsive to cues derived from the peripheral immune system, such as lymphocytes. Through this extensive bidirectional crosstalk, microglia regulate processes such as cytokine production, antigen presentation, phagocytosis, and synaptic pruning[1,3,4]. Although recent studies have demonstrated that systemic triggers can influence immune dynamics within the brain, our understanding of how real-world immune challenges impact microglial activity remains limited. Indeed, standard laboratory murine models raised under hygienic specific pathogen-free (SPF) conditions possess naïve and underdeveloped immune systems, characterized by low populations of effector and memory T and B cells, reduced immunoglobulin class switching, altered phenotypes of innate immune cells, and diminished or skewed inflammatory responses[5–7]. This limited exposure to natural microbes and complex antigens likely affects microglial states and functions.

The growing field of eco-immunology has shown that restoring natural antigenic diversity can recalibrate immune priming and maturation, thereby improving physiological and disease modeling in laboratory mice[8–10]. Strategies include wildling models[11,12], naturalization or feralization methods[5,13–16], and rewilding paradigms[17,18], all of which have shown that exposure to natural microorganisms and fomites promotes genuine immune development, comparable to that seen in wild-caught mice and adult humans[8,11,19,20]. Positive outcomes include increased resistance to pathogens, human-like immunization responses, and adapted inflammatory reactions across different organs such as the blood, spleen, gut, skin, and lungs.

Although these “dirty” modelling approaches reveal the critical role of antigenic diversity and complexity in shaping peripheral immunity, their impact on CNS-resident immune cells, particularly microglia, remains poorly characterized. One report has described how rewilding affects microglial activity in the context of fungal infection[21]. Whether environmentally driven immune maturation modulates microglial states in contexts of chronic neuroinflammation or neurodegenerative disease, such as Alzheimer’s disease (AD), remains unknown.

In AD, microglia transition from homeostatic surveillance states to disease-associated phenotypes (e.g., disease-associated microglia, DAM), characterized by altered gene expression, morphology, and function[22–24]. These activated microglial states play complex roles in the metabolism (e.g., phagocytosis, compaction, containment, and clearance) of pathological amyloid-β (Aβ) plaques and neuroinflammation[25–27]. Although recent studies indicate that peripheral stimuli can influence CNS immune responses and disease outcomes in SPF AD mice[28–30], it remains uncertain whether their immunological naïveté affects microglial transcriptional states and functions. This issue is vital for understanding the similarities and differences between murine and human AD microglial cells and, by extension, other immune cell responses[22,31–36].

In the current work, we employed a controlled indoor rewilding paradigm[37] to examine how a semi-natural farm-like environment influences peripheral and cerebral immune composition in wildtype (WT) and 5xFAD mice, a well-established transgenic model of Aβ pathology used in AD immunological research[38–43]. Our findings demonstrate that natural environmental exposure induces extensive immune maturation and remodeling, redirects brain transcriptional signatures towards those observed in human AD profiles, and reshapes Aβ-associated microglial responses. These findings position dirty mouse modeling as a potent driver of authentic neurodegenerative disease biology, offering a pathway toward more predictive, realistic, and human-relevant preclinical models.

RESULTS

Indoor rewilding recalibrates systemic leukocyte composition in WT and 5xFAD mice

To examine how indoor rewilding impacts systemic immunity in an Alzheimer's disease (AD) model, two-month-old SPF-born WT and 5xFAD female mice were randomly assigned to four experimental groups (**Figure 1B**). SPF cohorts (SPF-WT and SPF-5xFAD, N = 14 per genotype) were maintained in standard SPF animal facility conditions (IVCs). In parallel, rewilded cohorts (Rewild-WT and Rewild-5xFAD, N = 14 per genotype) were released into semi-natural enclosures (**Figure 1A**) for three months, a time period consistent with prior rewilding or naturalization studies[13,17,44]. To mimic natural *Mus musculus* habitats, the enclosures were enriched with a diverse array of organic and living biological elements, including farmland soil, plants, and arthropods, as described before[37]. No external pathogens are introduced using this method[37], and no mortality or health issues were observed in the current study. All animals were euthanized at five months of age (**Figure 1C**), corresponding to an early-to-mid stage of AD pathology in 5xFAD mice marked by Aβ plaque deposition, microglial activation, and neuroinflammation, yet preceding neurodegeneration or cognitive and motor decline[38,40,45]. Consistent with our previous findings[37], rewilded 5xFAD mice were, on average, 2.5g leaner than their SPF counterparts (not shown), likely reflecting increased physical activity and metabolic expenditure.

Rewilding increased the absolute abundance of $CD45^+$ leukocytes in both spleen and blood across genotypes (**Figure 2A,C**). In parallel, the fraction of $CD45^+$ cells among live events decreased under rewilding in both tissues, consistent with a housing-dependent shift in the overall composition of acquired suspensions. The magnitude of these effects differed by tissue, as the increase in $CD45^+$ abundance was more pronounced in blood than in spleen, whereas the reduction in $CD45^+$ frequency among live events was larger in spleen than in blood in absolute terms (percentage points). Notably, in 5xFAD mice, this decrease corresponded to ~37.5% and ~50% relative reductions in spleen and blood, respectively, consistent with a proportionally larger increase in non-$CD45^+$ live events under rewilding (**Figure 2A,C**).

In the spleen, rewilding strongly expanded the B-lineage compartment. Both $CD19^{+}CD138^{-}$ B cells and $CD138^{+}$ antibody-secreting cells (ASCs) increased under rewilding, not only as a fraction of $CD45^{+}$ leukocytes (**Figure 2B**; both $p<0.0001$) but also in absolute abundance (**Supplementary Figure 2A**; both $p<0.0001$), indicating that these changes reflect increased B-lineage cellular output rather than a purely compositional redistribution. Rewilding also increased innate lymphoid populations in spleen, with higher NK and NKT representation in both frequency (**Figure 2B**; NK $p=0.00075$; NKT $p<0.0001$) and abundance (**Supplementary Figure 2A**; both $p<0.0016$), consistent with coordinated expansion of these compartments.

In contrast, several myeloid-associated changes were primarily compositional within the spleen. $Ly6G^{+}$ cells decreased in frequency within $CD45^{+}$ leukocytes (**Figure 2B**; $p<0.0017$) while absolute $Ly6G^{+}$ abundance remained largely unchanged (**Supplementary Figure 2A**), consistent with a relative redistribution within the splenic leukocyte pool.

Similarly, other myeloid cells decreased substantially as a fraction of $CD45^{+}$ leukocytes in the spleen (**Figure 2B**; $p<0.0001$) without a corresponding decrease in absolute abundance (**Supplementary Figure 2A**), indicating that the reduced frequency largely reflects remodeling of the $CD45^{+}$ compartment rather than a net loss of these events. Notably, this compartment displayed an environment-dependent genotype pattern that reversed across housing conditions (SPF-WT > SPF-5xFAD; Rewild-WT < Rewild-5xFAD) (**Figure 2B**).

$CD11c^{+}$ cells showed a decrease that was more evident in WT under rewilding (**Figure 2B**; WT contrast $p=0.00011$), with only modest changes in abundance (**Supplementary Figure 2A**). $F4/80^{+}TREM2^{+}$ macrophages showed a modest downward trend in frequency with limited change in abundance.

In the blood, rewilding substantially increased circulating ASCs (frequency and abundance, both $p<0.0001$; **Figure 2D** and **Supplementary Figure 2B**). By contrast, $CD19^{+}CD138^{-}$ B-cell frequency was comparatively stable across environments, while absolute B-cell abundance increased under rewilding (**Supplementary Figure 2B**; $p<0.0017$). Importantly, $CD19^{+}CD138^{-}$ B-cell showed a genotype effect that increased under rewilding ($p=0.0004$ in frequency, and

p=0.01 in abundance). In addition, 5xFAD mice had significantly higher abundance (p=0.0086) and frequency (0.0023) of CD8+ cytotoxic T cells in SPF conditions, which was recalibrated to WT level under rewilding (**Figure 2D**, 5xFAD contrast p=0.0005). Notably, the $CD4^+/CD8^+$ T-cell ratio increased under rewilding conditions (**Figure 2D**; p<0.0076), consistent with a more pronounced regulatory tone within the blood compartment.

Blood myeloid populations showed distinct, genotype-dependent changes. $Ly6G^+$ cells increased in abundance under rewilding (**Supplementary Figure 2B**; p<0.036), accompanied by a significant frequency increase in 5xFAD (**Figure 2D**; environment contrast p=0.015). For other myeloids, frequency and abundance diverged across genotype in terms of frequency and abundance. Finally, CD11c+ cells showed similar pattern as in spleen with significant decrease in WT under rewilding (**Figure 2D**; WT contrast p=0.01). Taken together, these data show that indoor rewilding broadly remodels systemic immunity in both WT and 5xFAD mice, characterized by increased leukocyte abundance alongside pronounced shifts in leukocyte composition.

Rewilding increases B-cell activation and shifts CD38/IgD-defined subset states toward maturation

Within splenic $CD19^+CD138^-$ B lymphocytes, rewilding increased the fraction of cells positive for multiple activation-associated markers (**Figure 3A**). In particular, rewilding increased fractions of B cells positive for CD38, CD44, CD25. Rewilding also increased the fraction of B cells $CD44^{high}$ compared to SPF. Notably, the Rewild-WT group showed a significant decrease in the fraction of $CD86^+$ cells. In contrast, 5xFAD B cells exhibited a significant increase in the fraction of $CD335^+$ ($NKp46^+$) cells. Consistent with a differentiation shift, rewilding reduced the frequency of naïve B cells ($CD38^+IgD^+$) in spleen (**Figure 3B**; Environment effect shown in the adjacent interaction plot), while increasing germinal center-like B cells ($CD38^-IgD^-$) (**Figure 3C**; Environment effect) and memory-like B cells ($CD38^+IgD^-$) (**Figure 3D**; Environment effect; **Supplementary Figure 3A**). Notably, this latter subset showed marked population heterogeneity that was partitioned based on CD38 intensity and FSC-H (right plot, **Figure 3D**), motivating deeper quantification in Supplementary Figure 3. Phenotypically, these CD38/FSC-defined subfractions differed in expression (MFI) of CD19, CD38, CD44, and CD86. Importantly, there

were consistent genotype differences both in SPF and rewilding conditions (**Supplementary Figure 3B-D**).

Within the blood compartment, the differentiation shifts were similar to that in spleen, as rewilding increased fractions of $CD44^{+}$ and $CD44^{high}$, $CD25^{+}$ and $CD38^{+}$ (**Figure 3E**). In addition, circulating B lymphocytes decreased CD11c positivity in rewild conditions (**Figure 3E**). Similarly to splenic B cells, IgD^{+} frequencies were comparatively stable in blood (**Figure 3E**). Finally, rewilding decreased the frequency of naïve B cells ($CD38^{+}IgD^{+}$) in blood (**Figure 3F**) and increased memory-like B cells ($CD38^{+}IgD^{-}$) (**Figure 3G**), consistent with a systemic shift away from naïve phenotypes under rewilding.

Rewilding expands ASC output and shifts plasmablast/plasma-cell phenotypes toward a distinct activation/differentiation state in spleen and blood

In the spleen, rewilding strongly increased $MHCII^{+}CD19^{+}CD44^{high}$ plasmablasts abundance ($p<0.0001$) and increased their representation within the ASC compartment ($p<0.0001$), with similar effects in WT and 5xFAD (**Figure 4A**). Beyond expansion, splenic plasmablasts displayed coordinated, environment-linked remodeling of activation/differentiation markers. Under rewilding, plasmablasts showed higher CD38 and CD44 MFI together with a strong shift in MHCII MFI, consistent with a transition toward a more advanced marker-defined plasmablast state. Rewilding also induced a pronounced increase in CD25 MFI on plasmablasts (**Figure 4A**), indicating a distinct activation-associated phenotype within this compartment.

Consistent with this broader shift in ASC maturation state, splenic early plasma cells ($MHCII^{+}CD19^{-}CD44^{high}$) were strongly expanded under rewilding, both in abundance and as a fraction of ASCs (both $p<0.0001$; **Figure 4B**). Markedly, their marker intensities further emphasized separation from the plasmablast compartment. Relative to plasmablasts, early plasma cells showed lower MHCII and higher CD44 signal, and rewilding accentuated this pattern (**Figure 4B**). Notably, the MHCII signal of early plasma cells in SPF conditions approached the level observed in plasmablasts under rewilding, highlighting a compressed "maturation gap" between these compartments under rewilding exposure (**Figure 4A, B**).

In addition, splenic short-lived plasma cells (MHCII^{-}CD19^{-}CD44^{bright}) exhibited a genotype-dependent response to rewilding, with a pronounced increase in Rewild-5xFAD in both abundance and % of ASC compared with SPF-5xFAD and Rewild-WT (**Figure 4C**).

In contrast, plasmablast representation within circulating ASCs showed a weaker overall environment effect (p=0.091), yet displayed significant contrasts within WT (SPF-WT vs Rewild-WT p=0.001) and between rewilded genotypes (Rewild-WT vs Rewild-5xFAD p=0.002), consistent with a genotype-by-environment dependence captured by the interaction summary (I=2.23, **Figure 4D**). Importantly, circulating plasmablast phenotype was recalibrated under rewilding in 5xFAD mice. Under SPF conditions, 5xFAD plasmablasts displayed relatively higher CD19 and lower CD38 signal compared with SPF-WT, whereas under rewilding this pattern shifted toward the WT-like range through decreased CD19 and increased CD38, together with a coordinated shift in MHCII MFI across genotypes, consistent with a robust maturation effect of rewilding on both genotypes (**Figure 4D**). Finally, in contrast to spleen plasmablasts, CD86 MFI decreased in circulating plasmablasts under rewilding (**Figure 4D**), underscoring tissue-specific remodeling of activation-marker expression.

To determine whether rewilding-associated remodeling of circulating ASCs translated into altered humoral output, we quantified plasma immunoglobulin isotypes by MSD (**Supplementary Figure 4**). Baseline IgM levels showed a consistent genotype effect (WT > 5xFAD) in both SPF and rewilded conditions (SPF p=0.042; Rewild p=0.031), indicating a stable difference in the IgM compartment across environments. In contrast, rewilding selectively shifted isotypes as plasma IgA increased in both genotypes under rewilding (WT p=0.036; 5xFAD p=0.010), whereas IgG1 decreased under rewilding (WT, p=0.0086; 5xFAD, p=0.039). IgG2b and IgG2c remained essentially unchanged, consistent with mucosal immune activation rather than generalized systemic inflammation (**Supplementary Figure 4**). Together, spleen and blood data indicate that rewilding simultaneously increases ASC output and reshapes plasmablast/plasma-cell marker profiles in a compartment-dependent manner.

Indoor rewilding reshapes peripheral T-cell differentiation states

Because CD62L was not included in the T-cell panel, $CD8^+$ T-cell differentiation states were defined operationally using a hierarchical gating strategy (**Supplementary Figure 1**). After lineage exclusion and selection of $CD8a^+$ T cells, KLRG1 was used to separate $KLRG1^+$ short-lived effector-like $CD8^+$ cells (SLECs) from the $KLRG1^-$ compartment. Within $KLRG1^-$ $CD8^+$ cells, we further focused on a $CD127^+CD27^+$ precursor-enriched pool and partitioned this compartment by CD44 intensity using an FMO-based CD44 threshold to define $CD44^-$ (naïve), $CD44^+$ (virtual memory), and $CD44^{high}$ (MPEC) fractions. This CD44-based stratification captured a prominent environment-associated shift as rewilded mice displayed a clear rightward displacement of the CD44 distribution, with fewer $CD44^-$ events and enrichment of $CD44^+$, compared to SPF controls (**Figure 5A**).

In the spleen, rewilding shifted the $CD8^+$ compartment away from naïve states and toward antigen-experienced phenotypes (**Figure 5B**). The naïve $CD8^+$ fraction decreased in both genotypes, while the virtual memory fraction increased, consistent with the CD44 distribution shift observed in representative plots. Whereas the intermediate precursor (MPECs) and the most differentiated $CD8^+$ effector subset (SLECs) fractions showed more modest changes across environments, indicating that rewilding impacts early $CD8^+$ differentiation balance within secondary lymphoid tissue (**Figure 5B**). $CD4^+$ differentiation in spleen exhibited a genotype-selective remodeling pattern (**Figure 5C**). Rewilding reduced naïve $CD4^+$ representation while increasing central memory and effector-associated $CD4^+$ fractions in 5xFAD mice, consistent with an overall state more prone to shift toward more antigen-experienced $CD4^+$ states in AD mice. In contrast, regulatory $CD4^+$ T cells ($CD25^+CD127^-$) increased strongly under rewilding (**Figure 5C**) for both genotypes, indicating that rewilding robustly expands an immunoregulatory compartment within the spleen.

Within the blood, the rewilding-driven shift was particularly pronounced for $CD8^+$ T cells (**Figure 5D**). Rewilding strongly depleted the naïve $CD8^+$ and the virtual memory fractions in both genotypes, along with a modest increase in MPECS in 5xFAD mice ($p=0.025$). Notably, genotype differences apparent under SPF conditions were compressed under rewilding, as both genotypes shifted toward more antigen-experienced $CD8^+$ distributions (interaction plot, **Figure 5D**). In the circulating $CD4^+$ compartment, the principal detectable differentiation readout (naïve

$CD4^+$) was substantially reduced under rewilding (**Figure 5E**), mirroring the broader systemic shift away from naïve phenotypes. Together, these data show that indoor rewilding remodels T-cell differentiation balance in a tissue-dependent manner, with consistent depletion of naïve-like fractions and enrichment of antigen-experienced states

Indoor rewilding induces coordinated phenotype switching across peripheral innate myeloid compartments

To assess whether rewilding reprograms innate immune states, we quantified major splenic and circulating myeloid compartments and tracked their activation-marker profiles. A prominent feature of the rewilded spleen was the expansion of a distinct SSC^{low} neutrophil state (switched neutrophils) within the $Ly6G^+$ compartment (**Figure 6A**). This fraction increased strongly under rewilding ($p<0.0001$), whereas the conventional SSC^{high} neutrophil compartment showed the reciprocal shift (**Figure 6B**; $p<0.0001$). Importantly, this reconfiguration was accompanied by a coordinated marker remodeling consistent across both neutrophil states as indicated by pronounced environment-associated shifts in CD86, CD44, CD38, and CD25 MFIs. Markedly, SSC^{low} neutrophils were bright in CD38 and CD25 expression relative to SSC^{high} neutrophils, and decreased CD44 expression in rewilding conditions compared to SSC^{high} neutrophils (**Figure 6A, B**).

Beyond neutrophils, rewilding drove broad innate activation-marker remodeling across splenic antigen-presenting and monocyte/macrophage compartments. Conventional dendritic cells (cDCs; $CD11c^+MHCII^+$) increased under rewilding (**Figure 6C**; $p<0.0001$). Splenic RPM macrophages exhibited a strong reduction in their fraction (**Figure 6E**; $p<0.0001$) while simultaneously showing robust shifts in CD86/CD44/CD38 MFIs, consistent with major state remodeling within this macrophage niche (**Figure 6E**). Similarly, splenic patrolling monocytes increased (**Figure 6F**; $p<0.0071$) and showed strong rewilding-associated increases in CD38/CD25 MFIs while CD86 MFI strongly decreased, consistent with an activation-marker remodeling. Further, the broader monocyte-enriched compartment also increased in rewilding conditions (**Figure 6G**; $p<0.0061$).

A particularly striking and consistent pattern emerged for TREM2^{+} macrophages (F4/80^{+}SSC^{high}TREM2^{+}). While their frequency among leukocyte compartment did not show a strong overall environment effect (**Figure 6D**; $p<0.104$), their phenotype shifted dramatically. CD86 MFI decreased and TREM2 MFI increased under rewilding (**Figure 6D**), indicating a robust marker-defined reprogramming of this cell population.

In blood, the same "state switching" theme was detectable but generally more modest in magnitude. The SSC^{low} switched neutrophil fraction increased and the SSC^{high} conventional neutrophil decreased under rewilding (**Figure 6H**; both $p<0.006$), whereas other circulating myeloid compartments showed weaker or non-significant environment effects on frequency (**Figure 6H**). Notably, circulating TREM2^{+} macrophages again showed strong phenotype remodeling with substantially decreased CD86 and increased TREM2 MFIs despite limited changes in overall frequency (**Figure 6I**).

Taken together, peripheral immunophenotyping shows that indoor rewilding broadly remodels both adaptive and innate immune compartments in spleen and blood, coupling expansion of B-lineage/ASC output and shifts in T-cell differentiation with coordinated, marker-defined state changes across myeloid lineages. These consistent systemic effects in both WT and 5xFAD mice motivated us to next examine whether analogous remodeling is detectable within the brain.

Rewilding remodels brain microglial state balance and reprograms gene expression

Using CX3CR1 and P2RY12 to stratify brain microglia (**Figure 7A**), we quantified marker profiles in CX3CR1^{high}P2RY12^{high} (homeostatic-like) versus CX3CR1^{high}P2RY12^{dim} (reactive-like) microglial states (**Figure 7B, C**). Within both microglial states, rewilding was associated with a strong decrease in CX3CR1 and CD86 MFIs, and an increase in CD38 and CD25 MFIs, in both genotypes (**Figure 7B, C**). To minimize sensitivity to dissociation-related variation in total immune-cell yield, we assessed a homeostatic-like/reactive-like ratio within the CX3CR1^{high} compartment (**Figure 7D**). Rewilding increased this ratio within WT ($p=0.0029$), indicating a more homeostatic fraction relative to SPF-WT, consistent with WT-specific increase in P2RY12 MFI in rewilding conditions (**Figure 7B, C**).

In addition, qRT-PCR revealed robust rewilding-associated remodeling of inflammatory gene expression in 5xFAD mice (**Figure 7E**). With the exception of IL-1β, where the rewilding effect was significant in both genotypes, several other transcripts showed a strong environmental effect specific to 5xFAD mice. Indeed, in contrast to SPF-5xFAD mice, Rewild-5xFAD mice showed a tempered inflammatory profile, characterized by selective reductions in IL-1α, Ccl2, and IL-6, while IL-10, Nlrp3, and Tnf transcripts increased (**Figure 7E**). Similarly, two microglial disease-associated markers showed strong environment-linked changes. Clec7a and Itgax were strongly reduced in 5xFAD mice under rewilding conditions (**Figure 7F**), consistent with an attenuation of this DAM-related transcriptional axis.

Rewilding modulates microglia-Aβ interaction and metabolism

We next examined whether the microglial state shifts observed by flow cytometry and qRT-PCR were reflected in microglial morphology and in Aβ plaque-associated microglial physical interactions *in situ*. Microglia were classified into three Iba1-based morphological states (homeostatic, reactive, and amoeboid), illustrated by representative confocal images (**Figure 8A**). Quantitative classification uncovered pronounced effects of both genotype and environment, as well as significant G × E interactions on microglial distribution (**Figure 8B**). In the cortex, SPF 5xFAD mice displayed a clear shift toward a reactive state relative to SPF WT animals (genotype effect, $p<0.0001$), consistent with amyloid-driven activation. Rewilding partially normalized this profile, increasing the relative abundance of homeostatic and amoeboid microglia (Environment effect, $P<0.01$) and reducing the predominance of hypertrophied reactive cells (Interaction, $P<0.05$). Similar but attenuated effects were observed in the hippocampus, where environmental exposure broadened the morphological spectrum across genotypes, suggesting that microbial complexity expands the range of physiological activation states available to microglia. Given the strongest G × E interactions in the cortex, we further focused on this region.

Dual-labeling for Iba1 and Thioflavin S using high-resolution confocal imaging revealed a close spatial association between microglia and Aβ plaques, suggesting increased phagocytosis (**Figure 8C**). Quantitative 3D analysis of confocal z-stacks revealed that total microglial numbers per tissue volume were comparable between SPF-5xFAD and Rewild-5xFAD mice (**Figure 8D**).

However, while total Aβ plaque counts remained unchanged, rewilding significantly increased their mean volume (**Figure 8D**, p=0.0089), suggesting altered plaque dynamics or remodeling. Importantly, the density of reactive, plaque-associated microglia was significantly higher in 5xFAD-Rewild mice (**Figure 8D**, p=0.024). MSD quantification of human Aβ peptides showed that brain soluble and formic-acid insoluble $A\beta_{38/40/42}$ levels were broadly similar across groups, whereas plasma $A\beta_{42}$ was significantly reduced under rewilding (**Figure 8E**).

These findings suggest that rewilding alters microglial engagement and morphology in ways that support altered metabolic and surveillance functions. Microglia in naturalized environments seem to maintain a balanced state between resting and reactive modes, possibly enabling continuous plaque remodeling without worsening neuroinflammation. Overall, these results demonstrate how environmental microbial diversity could influence microglial structure and Aβ interactions, supporting a model where rewilding encourages adaptive immune-metabolic regulation rather than outright activation.

Rewilding redirects brain transcriptional signatures toward human Alzheimer's disease

To investigate how microbial exposure reshapes the brain transcriptome, we performed whole-brain Nanopore sequencing in SPF-WT, SPF-5xFAD, Rewild-WT, and Rewild-5xFAD mice, along with wild *Mus musculus* brains used as a natural reference (**Supplementary File 1**). Strikingly, indoor rewilding induced extensive transcriptional remodeling, with a 61% overlap of significant (± 1.25-fold-change, p<0.01) differently expressed genes (DEGs) between Rewild-WT and Wild-caught (Feral) mice (odds ratio = 2.94, $p=4.9\times10^{-219}$) when compared to SPF mice, demonstrating strong convergence of CNS gene expression toward wild-relevant physiological states (**Figure 9A**). Correlation analyses across differentially expressed gene contrasts further revealed that rewilding substantially redirected brain transcriptional programs, driving convergence across biological contexts. Rewild-WT mice shared a modest but significant correlation with Wild (Feral) mice (Pearson r=0.363, p=1.04e-62; n=1984 genes), indicating that environmental enrichment alone is sufficient to partially recapitulate feral transcriptional signatures (**Figure 9B**). Strikingly, the transcriptional profile of Rewild-WT mice showed a stronger correlation with SPF-5xFAD mice (r=0.748, p=1.03e-84; n=487), suggesting that rewilding and Alzheimer's-related pathology engage overlapping gene expression programs

(**Figure 9C**). This convergence was most pronounced in Rewild-5xFAD mice, which exhibited a near-complete correlation with Rewild-WT mice (r=0.962, p<1e-309; n=1976), demonstrating that the rewilding transcriptional signature dominates and is highly consistent regardless of genotype (**Figure 9D**).

We next quantified transcriptional changes of canonical markers (genes) across all major CNS lineages[46–51] (**Supplementary File 2**), where both environment and genotype exerted distinct effects relative to SPF-WT mice **(Figure 9E)**. SPF-5xFAD mice exhibited pronounced microgliosis, whereas rewilding significantly attenuated microglial activation. Oligodendrocytes, astrocytes, and endothelial cells showed moderate, directionally consistent remodelling, although OPCs were uniquely elevated in SPF-5xFAD. Pericytes and vascular smooth muscle cells (VSMC) remained largely unchanged across groups.

Pathway enrichment using KEGG (**Figure 9F**) and Ingenuity Pathway Analysis (IPA) (**Figure 9G**) revealed strong induction of immune, mitochondrial, oxidative phosphorylation, and antigen-presentation pathways in rewilded mice (**Supplementary File 3**). Notably, Rewild-5xFAD displayed substantially higher pathway activation scores than SPF-5xFAD, indicating synergistic effects of environmental complexity and amyloid pathology. Interestingly, among the top-scoring IPA "upstream regulators" of these pathways are immune (e.g., immunoglobulins, aducanumab) and AD (e.g., MAPT, APP, and PSEN1)-related genes (**Supplementary File 3**).

Quantitative gene expression analysis of canonical and emerging microglial states[52–54] reveals that SPF 5xFAD mice strongly activate DAM programs, as expected, alongside related Microglial NeuroDegenerative phenotype (MGnD), Axon Tract-associated Microglia (ATM), White matter–associated microglia (WAM), and phagocytic/lysosomal signatures, with concomitant loss of homeostatic features (**Figure 9H**). In contrast, rewilded WT (and Wild) mice also engage DAM-like programs but display stronger induction of antigen presentation, proteasomal, oxidative stress, and metabolic microglial states, consistent with immune conditioning. Importantly, rewilded 5xFAD mice exhibit a more diversified and attenuated degenerative microglial landscape, rather than a simple amplification of canonical DAM responses.

The expression analyses of individual AD-associated genes revealed that rewilding regulated several key human risk loci (e.g., Apoe, Trem2, Clu, and Picalm) (**Figure 10A-E**), strengthening the connection between ecological exposure and disease-relevant transcriptional networks. The modulatory effects of rewilding on selected microglial (Iba1) and astrocytic (Gfap) core genes could be reproduced at both mRNA and protein levels (**Figure 10B, D**).

Notably, cross-species pathway integration using IPA shows that rewilded 5xFAD mice, but not their SPF counterparts, exhibit transcriptional profiles that more closely align with bulk RNA-Seq human AD brain datasets[55] (entorhinal cortex and hippocampus) (**Figure 11D**). This effect was not observed in the human postcentral gyrus and superior frontal gyrus of AD individuals (**Supplementary File 3**), suggesting region-specific and Aβ-prone effects. Concordantly, engagement of the Human Alzheimer Microglia (HAM) signature[56], largely absent in SPF conditions, is strongly induced in rewilded and wild mice, together with increased overlap with bulk human AD brain expression profiles (**Figure 11E**). Collectively, these findings suggest that environmental microbial complexity reorients the murine CNS toward a transcriptional state that more closely resembles human AD.

DISCUSSION

This study demonstrates that ecological exposure profoundly restructures both peripheral and brain immune landscapes in WT and 5xFAD mice. By bridging the immunological sterility of SPF housing with lifelike microbial and antigenic complexity, our indoor rewilding approach restores key components of immune maturation, spanning effector, regulatory, and innate networks, and redefines the neuroimmune tone underlying Aβ-driven pathology. Together, these results establish dirty mouse modeling as an alternative, robust experimental framework for investigating how environmental complexity modulates systemic-neuroimmune crosstalk and disease progression, and for improving the translational fidelity of preclinical neurodegenerative disease research.

Our indoor rewilding platform[37], which bridges the concepts of (outdoor) rewilding and naturalization[13,44,57,58], offers a controlled ecosystem to promote natural microbial exposure in

laboratory mice. In line with previous dirty mouse models[5,19], our indoor rewilding recalibrated peripheral B- and T-cell populations toward phenotypes characteristic of immunological maturity, including expanded transitional and activated B cells, increased antibody-secreting cells, an enriched splenic $CD4^+$ Treg subset, and broad phenotypic shifts across differentiation and activation markers. This environmental "training" effectively corrects the immune immaturity typical of sterile SPF housing, moving the host from a naïve state toward antigen-experienced readiness[6,20]. Notably, the dominant $CD8^+$ T-cell profile observed in SPF-5xFAD mice was normalized to WT levels under rewilding, accompanied by an enhanced $CD4^+/CD8^+$ T-cell ratio in the blood and expansion of splenic Tregs. This suggests that a complex environment acts as a biological buffer, attenuating the extreme immune skewing driven by amyloid-related genetic mutations under isolated laboratory conditions, as shown in other genetic mouse models[18].

This adaptive immune recalibration was paralleled by a coordinated state-switch across innate immune cell populations, shifting them toward surveillance and the resolution of inflammation. The emergence of a $TREM2^{high}CD86^{low}$ macrophage signature is particularly notable. By downregulating CD86, a co-stimulatory molecule that drives inflammatory T-cell activation, while upregulating TREM2, a receptor central to debris recognition and clearance, these cells transition from pro-inflammatory sentinels to specialized effectors dedicated to tissue homeostasis and repair[24,46,59]. A parallel shift was observed in the neutrophil compartment, where rewilding downregulated CD86 and upregulated CD25, suggesting an immunomodulatory role. In this context, CD25 may act as a "molecular sink" that sequesters local IL-2, effectively limiting inflammatory amplification and promoting immune tolerance within the circulation, spleen, and likely other peripheral tissues such as the lungs[16,37].

Another defining feature of the rewilded immune phenotype is the robust, multi-lineage upregulation of CD38 across plasmablasts, neutrophils, macrophages, and monocytes. As an ecto-enzyme, CD38 catalyzes the hydrolysis of extracellular NAD^+, a damage-associated molecular pattern (DAMP) released during cellular stress and death. Its broad induction across immune lineages suggests that the rewilded immune system actively modulates extracellular NAD^+ levels to dampen stress signaling and regulate calcium-dependent activation, thereby

enhancing immune readiness while buffering against maladaptive inflammatory responses[60]. This global shift in NAD^+/calcium signaling regulation, combined with the expansion and accelerated maturation of antibody-secreting cells toward more advanced differentiation states, underscores an immune system that is highly responsive yet tightly regulated. Concordantly, the selective rise in plasma IgA rather than a generalized increase in pro-inflammatory IgG isotypes reflects a shift in the host's immune tone toward mucosal-associated immunity and active systemic regulation[5].

The peripheral immune recalibration observed under rewilding has direct implications for CNS immunity. The immunological naïveté of SPF mice can blunt host responses to both pathogens and therapeutics, limiting the fidelity of preclinical models[6]. By establishing a mature, integrated host immune environment, our indoor rewilding approach provides a higher-fidelity platform that better reflects the cumulative immune history of the human host. This mature peripheral landscape, marked by enhanced metabolic surveillance, expanded regulatory T cells, and a diversified myeloid repertoire, likely constitutes an essential prerequisite for the microglial plasticity and transcriptional remodeling we observed within the brain[4,61].

Within the CNS, rewilding did not simply suppress inflammation; rather, it diversified and recalibrated it. The rewilded brain exhibited an expanded cytokine repertoire that integrated both pro-inflammatory (IL-1β, IL-6, Ccl2) and regulatory (IL-10) mediators, consistent with a transition from the monolithic, DAM-driven activation characteristic of SPF-5xFAD mice toward a mixed, context-dependent immune state[3,53]. This transition was strikingly mirrored at the protein level, where the systemic immune signature induced by rewilding (decreased CD86 alongside increased CD38 and CD25) was recapitulated in microglial populations in the brain. This molecular convergence between peripheral and central compartments suggests that rewilding coordinates a systemic-to-neuroimmune coupling that prevents microglia from becoming entrapped in a chronic pro-inflammatory state, instead sustaining a homeostatic surveillance capacity even in the presence of amyloid pathology[61]. By attenuating DAM-associated transcripts such as Clec7a and Itgax (CD11c) while simultaneously amplifying regulatory mediators, including IL-10, rewilding recalibrates the neuroinflammatory response in 5xFAD mice toward a more adaptive phenotype[46]. Rather than simply dampening Aβ-associated

inflammation, microbial and antigenic exposure appears to "train" innate immune pathways, promoting responsiveness while preventing uncontrolled neurotoxicity. This challenges the traditional binary view of neuroinflammation as purely detrimental and aligns with the growing understanding that microglial function is not fixed by genetics alone but is dynamically shaped by peripheral immune cues and ecological context.

Our transcriptomic analyses reveal that microbial and antigenic diversity exerts profound regulatory control over neuroimmune and metabolic gene expression in the brain. Rewilding redirected brain transcriptional profiles toward those observed in wild-caught mice, and, in the context of amyloid pathology, toward signatures found in human AD, reflecting both convergence and compensation between environmental and genetic determinants of disease. The co-upregulation of Trem2-Clec7a modules that define DAM, coupled with enhanced expression of canonical homeostatic markers such as Gpr34, supports the notion that ecological exposure promotes a state of microglial plasticity: one in which microglia acquire the priming signals necessary to respond to pathological challenges without permanently forfeiting their homeostatic surveillance identity, a balance frequently lost in sterile SPF environments[61]. Importantly, these transcriptional signatures were accompanied by the upregulation of mitochondrial and lysosomal pathways, indicating increased bioenergetic and phagocytic capacity, features central to microglial adaptation in neurodegeneration[62,63].

Beyond microglial-specific programs, rewilding re-engaged oxidative phosphorylation, complement activation, and antigen-presentation modules, overlapping with molecular signatures found in human AD brains. Notably, rewilded 5xFAD mice, but not their SPF counterparts, exhibited transcriptional profiles that more closely aligned with human AD hippocampus and entorhinal cortex datasets, as evidenced by increased DEG overlap and stronger cross-species pathway concordance. This region-specific convergence (absent in the postcentral gyrus and superior frontal gyrus) suggests that rewilding preferentially amplifies Aβ-relevant and regionally localized transcriptional programs rather than inducing a generalized inflammatory response. While we used human transcriptional signatures from females (to match our mouse-based studies), similar associations were seen in age-matched males (data not shown). Correspondingly, the Human Alzheimer Microglia (HAM) signature, largely absent under SPF

conditions, was strongly induced in rewilded and wild mice, further underscoring the improved translational relevance of rewilded AD models. Together, these findings suggest that microbial and antigenic enrichment orchestrates a synchronized coupling between innate immune activation and metabolic adaptation, yielding a brain milieu that mirrors key molecular features of human AD while preserving dynamic regulatory control. Future studies integrating single-cell and spatial transcriptomics will be essential to delineate how environmental exposure reshapes immune-glial networks at the cellular level and to identify the circuits sustaining immune resilience.

Histological analyses confirmed that rewilding reprograms microglial morphology and Aβ engagement in ways consistent with the transcriptional data. In SPF-5xFAD brains, microglia predominantly displayed hypertrophied morphologies with thickened, shortened processes, a hallmark of metabolic strain and inflammatory entrenchment[62]. By contrast, rewilding diversified microglial architecture, restoring populations of ramified and intermediate forms indicative of sustained surveillance competence[2]. Plaque-associated microglia were not numerically increased, yet showed significantly enhanced reactive microglial density per plaque, suggesting greater per-cell phagocytic engagement[64]. Whether this heightened physical interaction translates into net amyloid clearance remains an open question of temporal dynamics. Our 3-month rewilding protocol likely captures the re-education and recruitment phase of the neuroimmune response, in which microglia are metabolically primed but have not yet reached the threshold for significant plaque dissolution. The increased microglial engagement observed without a concomitant reduction in plaque volume may alternatively reflect restoration of the "microglial barrier," wherein microglia tightly encapsulate plaques to limit the diffusion of toxic Aβ oligomers toward surrounding neurites[64]. This model is consistent with the observed increase in mean plaque volume without a change in plaque count, suggesting altered plaque compaction dynamics rather than net accumulation. We therefore hypothesize that sustained systemic immune priming over a more prolonged period, mimicking chronic lifelong microbial exposure, may be required to convert this enhanced microglial engagement into measurable Aβ clearance.

The systemic-to-central immune interactions observed in this study point to a state of immunological resilience induced by rewilding, characterized by a dynamic equilibrium between

activation and regulation. This contrasts sharply with the hyperreactive inflammatory milieu of SPF 5xFAD mice, where immune immaturity and exaggerated innate cascades may distort disease mechanisms and weaken translational fidelity. Such divergence likely contributes to the recurrent disconnect between preclinical outcomes and clinical reality, exemplified by the limited bench-to-bedside success of anti-Aβ immunotherapies and the emergence of amyloid-related imaging abnormalities (ARIA) in human trials. In humans, the neurovascular unit and blood-brain barrier operate within a mature immune milieu that is largely absent in SPF mice, potentially leading to systematic underestimation of vascular side effects associated with aggressive plaque clearance strategies[65,66]. These results highlight the need for AD models that better capture human immune complexity. While emerging systems such as cerebral organoids and iPSC-derived microglia xenografts offer powerful platforms for dissecting human-specific genetic mechanisms, they largely operate outside the organism-level context that shapes brain-immune interactions *in vivo*[67,68]. Our indoor rewilding framework is intended as a complementary, paradigm-level shift: rather than "humanizing" isolated cells in sterile settings, it reintroduces controlled ecological exposure to whole organisms to better align CNS pathology with a lifetime of systemic immune conditioning.

Future directions should focus on defining the causal microbial and antigenic drivers of brain immune plasticity and delineating how they interact with genetic AD risk factors such as Apoe and Trem2. Identifying the specific microbiome configurations, dietary components, and environmental signals that mediate neuroimmune reprogramming may enable precision rewilding strategies that enhance translational validity while maintaining experimental rigor. Additionally, exploring the roles of the circadian cycle, temperature, and other environmental variables[69] may further refine the rewilding framework. Expanding this approach to other neurodegenerative pathologies, including Tau pathology, neurovascular dysfunction, and synucleinopathies, as well as to humanized AD risk models (e.g., APOE4, TREM2 variants) will be essential for determining the generalizability of rewilding-driven neuroimmune effects. In this way, environmental microbial complexity could become not merely a confounding variable to control, but a biological parameter to actively harness in the design of more predictive and ecologically grounded preclinical studies.

This study has several limitations. First, rewilded mice were exposed simultaneously to increased environmental complexity, greater physical activity, and a more diverse diet, each of which can independently influence AD-related outcomes. Although food intake was not quantitatively assessed, WT and 5xFAD mice were housed within the same enclosures under identical conditions, mitigating major environmental and dietary confounders between genotypes. Second, behavioral and cognitive performance were not directly evaluated in the current study, although our previous work with this rewilding platform[37] demonstrated improvements in neuromotor and respiratory performance, and similar benefits might reasonably be expected here. Third, all animals were female, and sex-specific effects of rewilding on neuroimmune programming remain to be examined. Finally, the 3-month rewilding window, while sufficient to induce substantial immune and transcriptional remodeling, may not fully capture the long-term dynamics of microglial adaptation and amyloid clearance. Future investigations should systematically address how the duration of rewilding exposure, as well as age at onset, genetic background, and disease stage, modulate its neuroimmune effects.

In conclusion, this study provides the first comprehensive evidence that dirty mouse modeling reshapes neuroimmune and neuropathological processes within the CNS of a transgenic AD model. It establishes a foundation for exploring how ecological context intersects with the genetic and molecular determinants of AD, thereby bringing preclinical research closer to the real-world complexity of biological systems. Our findings extend the rewilding paradigm beyond systemic immunity, demonstrating that environmental microbial diversity reconfigures neuroimmune networks across multiple biological scales, from circulating lymphocytes to brain-resident microglia, and brings the transcriptional landscape of AD mice measurably closer to human disease. Ultimately, these insights may guide the development of more predictive, humane, and ecologically grounded experimental systems for studying and treating neurodegenerative diseases.

MATERIALS AND METHODS

Ethics statement

All procedures involving mice were carried out in accordance with the Canadian Council on Animal Care (CCAC) guidelines and were approved by the Animal Care Committee (CPAUL-2, approval number: 2024-1540). Female mice were chosen to reduce confounding factors related to breeding and limit aggression within the vivarium.

Laboratory mice

Female 5xFAD transgenic mice (C57BL/6J genetic background; strain #034840-JAX; B6.Cg-Tg(APPSwFlLon,PSEN1*M146L*L286V)6799Vas/Mmjax) aged 6 weeks and their age-matched female wild-type (WT) littermates were purchased from MMRCC. After 2 weeks of housing under SPF laboratory conditions, the mice were weighed and randomly assigned to four experimental groups. The first two groups (SPF-WT and SPF-5xFAD) were kept under SPF conditions, while the other two groups (Rewild-WT and Rewild-5xFD) were transferred to the indoor vivarium for rewilding. All groups were housed at ~22°C and ~45%RH under a 12:12-hour light/dark cycle, with food and water provided *ad libitum*. After three months, rewilded mice were recaptured using Havahart-type live traps. The vivarium environment, capture procedures, and post-capture handling were performed as previously described[37]. Finally, mice were weighed and euthanized concurrently with the SPF-housed mice.

Wild-caught mice

Wild mice were captured in rural Québec City, Canada, using Longworth traps, which are specifically designed for the live capture of small mammals. Traps were set in the evening and left in place overnight at various strategic locations around a familial farm, including near garbage bins, at the entrances of buildings (the owner's house, the sugar shack, the barn, the agricultural storage building, and the stable), and along structures where prior signs of murine activity had been observed. Traps were inspected early in the morning, and captured female mice were transported to the laboratory.

Tissue collection and plasma preparation

All mice in this study were euthanized by decapitation without prior anesthesia, in accordance with institutional animal care and use guidelines and approved ethical protocols. Trunk blood was immediately collected into EDTA-coated tubes. For the N=8 cohort (see **Figure 1C**), a fraction of whole blood was kept fresh for flow cytometry, while the remainder was centrifuged (2000×g, 10 min, 4°C). The resulting plasma was aliquoted and stored at -80°C for subsequent MesoScale Discovery (MSD) assays (immunoglobulins and $A\beta_{40/42}$). Brains were rapidly harvested and mid-sagittally hemisected. For the N=8 cohort, the right hemisphere and the spleen were processed fresh for cellular dissociation and flow cytometry. The left hemisphere was snap-frozen and cryo-milled on dry ice to be processed for qRT-PCR, Western blot, and MSD-based Aβ quantification (soluble and insoluble fractions of $A\beta_{38}$, $A\beta_{40}$, and $A\beta_{42}$). For the transcriptomics and morphology cohort (N=6 cohort; see **Figure 1C**), the left hemisphere was processed for Nanopore sequencing, while the right hemisphere was fixed for immunohistochemistry (IHC) and morphological analysis.

Flow cytometry

All samples were maintained on ice (in ice-cold 1xPBS for brain and spleen) until further processing. Single-cell suspensions were generated from each tissue and stained with fluorochrome-conjugated antibodies (**Supplementary Table 1**). Data were acquired using an Aurora spectral flow cytometer (Cytek Biosciences) and analyzed using FlowJo v10 software. Gating strategies were established based on fluorescence fluorescence-minus-one (FMO) controls and are presented in **Supplementary Figure 1A** and **1B**. Statistical analyses for flow cytometry were performed in R (RStudio 2026.01.0+392). Prior to modeling, outliers were systematically identified and excluded within each experimental group using a robust Z-score method based on the median absolute deviation (threshold $|Z|>3.5$). To satisfy the assumptions of normality and homoscedasticity, cell abundance data were log(1+x) transformed, while population frequencies were logit-transformed. Median Fluorescence Intensity (MFI) values were normalized using an arcsinh transformation with a cofactor of 150. Statistical significance (defined at $p<0.05$) was assessed using linear models incorporating Genotype, Environment, and their interaction. Pre-specified simple contrasts were extracted using estimated marginal means (EMMeans). All p-values were derived from the global model's pooled residual error to ensure a robust estimate of variance across all experimental groups. For selected panels, GraphPad Prism

v10 was used to generate interaction plots and to fit two-way ANOVA full models for visualization of main effects and interactions (E, G, I reported as $-\log_{10}(P)$ where indicated). Ratio metrics were analyzed after Log_{10}-transformation, with raw ratio values displayed in figures where indicated.

RNA extraction and quantitative RT-PCR

Around 80mg of cryo-milled brain was used for total RNA extraction with TRIzol Reagent (Life Technologies), according to the manufacturer's instructions. RNA concentration and purity were assessed using a NanoQuant plate spectrophotometer (Infinite 2000, TECAN). Complementary DNA (cDNA) was synthesized from 2 µg of total RNA using the High-Capacity cDNA Reverse Transcription Kit (Thermo Fisher Scientific, Cat# 4368814). qRT-PCR reactions were performed using 30 ng of cDNA using PowerTrack SYBR Green Master Mix (Thermo Fisher Scientific, Cat#A46109) on a LightCycler 480 II system (Roche). Primer sequences (1 µM each) are listed in (**Supplementary Table 2**), and their specificity was verified using NCBI Primer-BLAST. The amplification protocol consisted of the following steps: 50°C 2min, 95°C 10min, [95°C 30sec, 60°C 30sec] x40, 95°C 1min, 55°C 30sec, 95°C 30sec. Relative gene expression levels were determined using the $2^{-\Delta\Delta Ct}$ method, using endogenous Gapdh as a normalization gene. Data were $\log_2$-transformed prior to statistical analysis using GraphPad prism v10.

Nanopore RNA Sequencing

Total RNA (2µg per sample) was extracted from the left brain hemisphere as described above and sent to the Integrated Genomics Meta-Platform at CHU Sainte-Justine (Montréal, QC, Canada) for bulk (whole tissue) sequencing. Libraries were prepared from total extracted RNA using the cDNA-PCR sequencing kit (SQK-PCB114-24) from Oxford Nanopore. The samples were loaded onto 3 FLO-PRO114M flow cells and sequenced PromethION 24 at the CRA-CHUSJ Integrated Genomics Meta-Platform (MPGI) for 72 hours. Pod5 files were base called with Dorado v.0.8.0 (Oxford Nanopore Technologies) using model sup@v5.0.0. Reads with a Phred Q score of 10 or more were kept for downstream analysis. Transcripts quantification and alignment were done using oarfish v.0.6.5 [70] and Mus musculus GRCm39 reference transcriptome with parameters '--seq-tech ont-cdna', '--filter-group no-filters' and '--model-

coverage'. Differential expression analysis was done using the R package DESeq2 v.1.48.2 [71] and counts were normalized with the default method, median of ratios.

Protein extraction and immunoblotting

Cryo-milled brain was used to isolate soluble and insoluble protein fractions. Specifically, 100 mg of frozen brain powder were lysed in RIPA buffer composed of 50 mM Tris–HCl (pH 8), 150 mM NaCl, 1% Nonidet P-40, 0.5% sodium deoxycholate, 0.1% SDS, 1 mM phosphatase inhibitors, 1 mM PMSF, and one Complete Mini EDTA-free protease inhibitor tablet (Roche Life Science). Lysates were centrifuged at 100,000×g for 20 min at 4 °C, and the supernatant containing the soluble fraction was collected. The remaining pellet, representing the insoluble fraction, was resuspended in 70% formic acid and centrifuged at 25,000×g for 20 min at 4 °C. The resulting supernatant was evaporated under a fume hood for three days, and the dried residue was resuspended in 5M guanidine hydrochloride diluted in 0.05M Tris–HCl (pH 8). Protein concentrations were quantified using the Pierce BCA Protein Assay Kit (ThermoFisher Scientific). For immunoblotting, 20µg of protein per sample were resolved on 15% SDS–PAGE gels and transferred onto nitrocellulose membranes (Bio-Rad). Membranes were blocked for 1 h at room temperature with 5% non-fat dry milk in TBS containing 0.1% Tween-20, followed by overnight incubation at 4 °C with the appropriate primary antibodies (listed in **Supplementary Table 3**). After washing, membranes were incubated with HRP-conjugated secondary antibodies and developed using the Immobilon® ECL UltraPlus Western HRP Substrate (Millipore). Total protein staining (Ponceau S) was used for normalization. Signals were visualized using a ChemiDoc Imaging System (Bio-Rad), and densitometric quantification was performed with ImageJ software (version 1.53). Statistical analysis used GraphPad prism v10.

Multiplex MSD quantification of Amyloid beta and immunoglobulins

The quantification of human amyloid beta peptides, Aβ38, Aβ40, and Aβ42, in the brain was performed using the V-PLEX Aβ Peptide Panel 1 kit 6E10 (#K15200E, Meso Scale Discovery, Maryland, USA). Whereas the quantification of human amyloid beta peptides, Aβ40 and Aβ42, in the plasma was performed using the R-PLEX 4G8 kit (#L45SA-1; #F209M-3; #K1509MR-2; #K1509LR-2; #F209L-3). The quantification of plasma immunoglobulins was performed using the T-PLEX Mouse Isotyping Panel 1 (IgA, IgG1, IgG2a/c, IgG2b, IgG3, IgM) (#K15183B). All

procedures were according to the manufacturer's instructions. Plates were read on a MESO® QuickPlex SQ-120 Multiplex imager. Data were analyzed using MSD-Workbench software. Results were log_{10}-transformed prior to statistical analysis to account for skewed distributions, using GraphPad prism v10.

Immunofluorescence

The right brain hemispheres (N=6 per group) were fixed in 4% paraformaldehyde (PFA) for 12h and then transferred to PBS-sucrose 30% for 24h for cryopreservation. The half-brains were then transferred to isopentane at -40°C on dry ice for 10s for rapid freezing. The half brains were kept at -80°C until cold sectioning with a cryostat microtome (thickness, 16 mm). The resulting cryosections were preserved from contamination in PBS-Azide 0.2% until immunostaining. Cryosections were rinsed three times in PBS, followed by successive immersions in 70% and 80% ethanol, Thioflavin S (T1892-25G, Sigma Aldrich, USA) was prepared at 1% in 80% ethanol, and the solution was syringe-filtered to remove any undissolved particles. Slides were then incubated in the Thioflavin S solution for 15 minutes at room temperature under agitation, protected from light. After incubation, slides were rinsed sequentially in 80% and 70% ethanol followed by two washes in PBS. Sections were subsequently permeabilized with PBS-Triton 0.2% and saturated with Normal Goat Serum 1/100 (Vector Laboratories; Cat. No. S-1000) for one hour at room temperature and then labeled with primary antibodies anti-Iba1 1/500 (Rabbit, #019-19741, Wako). Afterwards, sections were incubated with secondary antibodies goat anti-rabbit 568 1/500 (#A11036, Invitrogen) for 1 hour at RT. The sections were then incubated with DAPI (D1306, Invitrogen) and bathed in 70% ethanol and Sudan black (Sigma, Canada) to eliminate autofluorescence. The sections were then mounted on Superfrost slides (ThermoFisher) using Fluoromount-GTM Mounting Medium (Invitrogen, 00495802). The slides were finally digitized using a slide scanner (Axioscan Z1, Zeiss).

Image analysis

High-resolution images obtained from the slide scanner were analyzed using a flexible algorithm developed by the imaging platform of our research center under MathWorks MATLAB 2018b software. Briefly, the code includes a multi-CPU-GPU batch image processor that reads raw images, microscope metadata, and experimental factors to serve 4D matrices to a custom plugin

written to detect 3D objects labeled in red (microglia) and green (Aβ plaques). This automated pipeline quantified, within the cortex (C) and the hippocampus (HX), the object properties such the size, the number, and the fluorescence intensities. The property values were aggregated along samples and groups to produce tissue measurements in terms of means ± standard error of the mean (SEM). Object intersections were determined from voxel lists to get microglia-plaque colocalization. The plugin further distinguished distinct microglial morphologies based on soma size and ramification complexity (Homeostatic, Reactive, Amoeboid), providing an integrated assessment of microglial activation states. All quantitative measures were normalized to the analyzed mask volume. Group comparisons were performed using an ANOVA 2-way statistical test at 5% *p*-value threshold followed by a Holm-Bonferroni post-hoc test under OriginLab (OriginPro 2015 software).

Patient and public involvement

Patients and/or the public were not involved in the design, conduct, reporting, or dissemination plans of this research.

Funding statement

This work was supported by the Canadian Institute of Health Research (CIHR), the Natural Sciences and Engineering Research Council of Canada (NSERC), and the *Fonds de Recherche du Québec en Santé* (FRQS).

Acknowledgements

We thank all family members of *La ferme du vieux caveau* farm located in Saint-Joachim, Québec, for generously providing soil and other organic materials for our indoor enclosures and for allowing us to capture Wild mice. We also thank Sébastien Poulin and all staff members of the IUCPQ animal facility for their support and guidance. Our gratitude extends further to the CRCHUQ animal facility team for their continuous assistance. Finally, we thank Vincent Desrosiers from the cytometry platform at the CHU de Québec-Université Laval Research Center for guidance and data analysis.

CRediT authorship contribution statement

Mohamed Lala Bouali: conceptualization, methodology, investigation, formal analysis, visualization, data curation, writing - original draft, writing - review & editing of the final manuscript. **Amir Mohamed Kezai**: conceptualization, methodology, investigation, formal analysis, writing - original draft. **Marc Bazin:** formal analysis. **Papa Yaya Badiane**: investigation. **Nasim Eskandari**: investigation. **Véronique Lévesque**: investigation. **Justin Robillard**: resources. **Denis Soulet**: resources. **Cyntia Tremblay**: investigation. **Frédéric Calon**: resources. **Françoise Morin**: investigation, formal analysis. **Luc Vallières**: resources, formal analysis, validation. **Sébastien S. Hébert**: funding acquisition, conceptualization, project administration, resources, supervision, validation, data curation, formal analysis, visualization, writing - review & editing of the final manuscript. All the authors have read and approved the final manuscript.

Competing interests

The authors declare that they have no competing interests.

Materials & Correspondence

The authors confirm that the datasets, including raw data, supporting the findings of the current study, are available from the corresponding author. The raw Nanopore FASTQ files were unexpectedly lost during manuscript preparation due to circumstances beyond the authors' control. Processed data, including normalized gene-expression matrices, are provided with this manuscript and remain fully available for review. All corresponding tissue specimens and extracted total RNA are preserved and can be used to regenerate sequencing datasets upon reasonable request to the corresponding author.

ORCID iDs

Mohamed Lala Bouali (Lala Bouali M.): https://orcid.org/0000-0002-4995-5604
Sébastien S. Hébert (Hébert S.S.): https://orcid.org/0000-0002-0391-9325
Luc Vallières (Vallières L.): https://orcid.org/0000-0002-0737-1539
Véronique Lévesque (Lévesque V.): https://orcid.org/0009-0003-5583-0829

REFERENCES:

1. Zengeler KE, Lukens JR. Innate immunity at the crossroads of healthy brain maturation and neurodevelopmental disorders. *Nat Rev Immunol*. 2021;21(7):454-468. doi:10.1038/s41577-020-00487-7

2. Mayer MG, Fischer T. Microglia at the blood brain barrier in health and disease. *Front Cell Neurosci*. 2024;18. doi:10.3389/fncel.2024.1360195

3. Müller L, Di Benedetto S, Müller V. The dual nature of neuroinflammation in networked brain. *Front Immunol*. 2025;16. doi:10.3389/fimmu.2025.1659947

4. Passaro AP, Lebos AL, Yao Y, Stice SL. Immune Response in Neurological Pathology: Emerging Role of Central and Peripheral Immune Crosstalk. *Front Immunol*. 2021;12. doi:10.3389/fimmu.2021.676621

5. Beura LK, Hamilton SE, Bi K, et al. Normalizing the environment recapitulates adult human immune traits in laboratory mice. *Nature*. 2016;532(7600):512-516. doi:10.1038/nature17655

6. Tao L, Reese TA. Making Mouse Models That Reflect Human Immune Responses. *Trends Immunol*. 2017;38(3):181-193. doi:10.1016/j.it.2016.12.007

7. Burger S, Stenger T, Pierson M, et al. Natural Microbial Exposure from the Earliest Natural Time Point Enhances Immune Development by Expanding Immune Cell Progenitors and Mature Immune Cells. *J Immunol*. 2023;210(11):1740-1751. doi:10.4049/jimmunol.2300061

8. Graham DM. A walk on the wild side. *Lab Anim*. 2017;46(11):423-427. doi:10.1038/laban.1372

9. Flies AS, WILD COMPARATIVE IMMUNOLOGY CONSORTIUM. Rewilding immunology. *Science*. 2020;369(6499):37-38. doi:10.1126/science.abb8664

10. Viney M, Lazarou L, Abolins S. The laboratory mouse and wild immunology. *Parasite Immunol*. 2015;37(5):267-273. doi:10.1111/pim.12150

11. Rosshart SP, Herz J, Vassallo BG, et al. Laboratory mice born to wild mice have natural microbiota and model human immune responses. *Science*. 2019;365(6452):eaaw4361. doi:10.1126/science.aaw4361

12. Runge S, von Zedtwitz S, Maucher AM, et al. Laboratory mice engrafted with natural gut microbiota possess a wildling-like phenotype. *Nat Commun*. 2025;16(1):5301. doi:10.1038/s41467-025-60554-2

13. Arnesen H, Knutsen LE, Hognestad BW, et al. A Model System for Feralizing Laboratory Mice in Large Farmyard-Like Pens. *Front Microbiol*. 2021;11. doi:10.3389/fmicb.2020.615661

14. Arnesen H, Birkeland S, Stendahl H, et al. Comparison of naturalization mouse model setups uncover distinct effects on intestinal mucosa depending on microbial experience. *Discov Immunol*. 2025;4(1):kyaf002. doi:10.1093/discim/kyaf002

15. Arnesen H, Markussen T, Birchenough G, et al. Microbial experience through housing in a farmyard-type environment alters intestinal barrier properties in mouse colons. *Sci Rep*. 2023;13(1):13701. doi:10.1038/s41598-023-40640-5

16. Block KE, Iijima K, Pierson MJ, et al. Physiological microbial exposure transiently inhibits mouse lung ILC2 responses to allergens. *Nat Immunol*. 2022;23(12):1703-1713. doi:10.1038/s41590-022-01350-8

17. Leung JM, Budischak SA, The HC, et al. Rapid environmental effects on gut nematode susceptibility in rewilded mice. *PLOS Biol*. 2018;16(3):e2004108. doi:10.1371/journal.pbio.2004108

18. Lin JD, Devlin JC, Yeung F, et al. Rewilding Nod2 and Atg16l1 Mutant Mice Uncovers Genetic and Environmental Contributions to Microbial Responses and Immune Cell Composition. *Cell Host Microbe*. 2020;27(5):830-840.e4. doi:10.1016/j.chom.2020.03.001

19. Abolins S, King EC, Lazarou L, et al. The comparative immunology of wild and laboratory mice, Mus musculus domesticus. *Nat Commun*. 2017;8(1):14811. doi:10.1038/ncomms14811

20. Oh JH, Rehermann B. Natural versus Laboratory World: Incorporating Wild-Derived Microbiota into Preclinical Rodent Models. *J Immunol*. 2021;207(7):1703-1709. doi:10.4049/jimmunol.2100426

21. Yeung F, Chen YH, Lin JD, et al. Altered immunity of laboratory mice in the natural environment is associated with fungal colonization. *Cell Host Microbe*. 2020;27(5):809-822.e6. doi:10.1016/j.chom.2020.02.015

22. Zhou Y, Song WM, Andhey PS, et al. Human and mouse single-nucleus transcriptomics reveal TREM2-dependent and TREM2-independent cellular responses in Alzheimer's disease. *Nat Med*. 2020;26(1):131-142. doi:10.1038/s41591-019-0695-9

23. Frigerio CS, Wolfs L, Fattorelli N, et al. The Major Risk Factors for Alzheimer's Disease: Age, Sex, and Genes Modulate the Microglia Response to Aβ Plaques. *Cell Rep*. 2019;27(4):1293-1306.e6. doi:10.1016/j.celrep.2019.03.099

24. Deczkowska A, Keren-Shaul H, Weiner A, Colonna M, Schwartz M, Amit I. Disease-Associated Microglia: A Universal Immune Sensor of Neurodegeneration. *Cell*. 2018;173(5):1073-1081. doi:10.1016/j.cell.2018.05.003

25. Rangaraju S, Dammer EB, Raza SA, et al. Identification and therapeutic modulation of a pro-inflammatory subset of disease-associated-microglia in Alzheimer's disease. *Mol Neurodegener*. 2018;13(1):24. doi:10.1186/s13024-018-0254-8

26. Lee CYD, Daggett A, Gu X, et al. Elevated TREM2 Gene Dosage Reprograms Microglia Responsivity and Ameliorates Pathological Phenotypes in Alzheimer's Disease Models. *Neuron*. 2018;97(5):1032-1048.e5. doi:10.1016/j.neuron.2018.02.002

27. Gao C, Jiang J, Tan Y, Chen S. Microglia in neurodegenerative diseases: mechanism and potential therapeutic targets. *Signal Transduct Target Ther*. 2023;8(1):359. doi:10.1038/s41392-023-01588-0

28. Lu Y, Saibro-Girardi C, Fitz NF, et al. Multi-transcriptomics reveals brain cellular responses to peripheral infection in Alzheimer's disease model mice. *Cell Rep*. 2023;42(7). doi:10.1016/j.celrep.2023.112785

29. Seo D oh, Holtzman DM. Current understanding of the Alzheimer's disease-associated microbiome and therapeutic strategies. *Exp Mol Med*. 2024;56(1):86-94. doi:10.1038/s12276-023-01146-2

30. Guerrero-Carrasco M, Targett I, Olmos-Alonso A, Vargas-Caballero M, Gomez-Nicola D. Low-grade systemic inflammation stimulates microglial turnover and accelerates the onset of Alzheimer's-like pathology. *Glia*. 2024;72(7):1340-1355. doi:10.1002/glia.24532

31. Sun N, Victor MB, Park YP, et al. Human microglial state dynamics in Alzheimer's disease progression. *Cell*. 2023;186(20):4386-4403.e29. doi:10.1016/j.cell.2023.08.037

32. Olah M, Menon V, Habib N, et al. Single cell RNA sequencing of human microglia uncovers a subset associated with Alzheimer's disease. *Nat Commun*. 2020;11(1):6129. doi:10.1038/s41467-020-19737-2

33. Prater KE, Green KJ, Mamde S, et al. Human microglia show unique transcriptional changes in Alzheimer's disease. *Nat Aging*. 2023;3(7):894-907. doi:10.1038/s43587-023-00424-y

34. Guvenek A, Parikshak N, Zamolodchikov D, et al. Transcriptional profiling in microglia across physiological and pathological states identifies a transcriptional module associated with neurodegeneration. *Commun Biol*. 2024;7(1):1168. doi:10.1038/s42003-024-06684-7

35. Mallach A, Zielonka M, Lieshout V van, et al. Microglia-astrocyte crosstalk in the amyloid plaque niche of an Alzheimer's disease mouse model, as revealed by spatial transcriptomics. *Cell Rep*. 2024;43(6). doi:10.1016/j.celrep.2024.114216

36. Chen Y, Colonna M. Microglia in Alzheimer's disease at single-cell level. Are there common patterns in humans and mice? *J Exp Med*. 2021;218(9):e20202717. doi:10.1084/jem.20202717

37. Lala Bouali M, Kezai AM, Beaulieu MJ, et al. Indoor rewilding of laboratory mice recalibrates pulmonary mucosal immunity and mechanics. *Mucosal Immunol*. 2026;0(0). doi:10.1016/j.mucimm.2026.02.003

38. Eimer WA, Vassar R. Neuron loss in the 5XFAD mouse model of Alzheimer's disease correlates with intraneuronal Aβ42 accumulation and Caspase-3 activation. *Mol Neurodegener*. 2013;8(1):2. doi:10.1186/1750-1326-8-2

39. Landel V, Baranger K, Virard I, et al. Temporal gene profiling of the 5XFAD transgenic mouse model highlights the importance of microglial activation in Alzheimer's disease. *Mol Neurodegener*. 2014;9(1):33. doi:10.1186/1750-1326-9-33

40. Forner S, Kawauchi S, Balderrama-Gutierrez G, et al. Systematic phenotyping and characterization of the 5xFAD mouse model of Alzheimer's disease. *Sci Data*. 2021;8(1):270. doi:10.1038/s41597-021-01054-y

41. Shabestari SK, Morabito S, Danhash EP, et al. Absence of microglia promotes diverse pathologies and early lethality in Alzheimer's disease mice. *Cell Rep*. 2022;39(11). doi:10.1016/j.celrep.2022.110961

42. Xu Z, Kiani Shabestari S, Barannikov S, et al. Microglia-specific regulation of lipid metabolism in Alzheimer's disease revealed by microglial depletion in 5xFAD Mice. *Nat Commun*. 2025;16(1):9156. doi:10.1038/s41467-025-64161-z

43. Spangenberg E, Severson PL, Hohsfield LA, et al. Sustained microglial depletion with CSF1R inhibitor impairs parenchymal plaque development in an Alzheimer's disease model. *Nat Commun*. 2019;10(1):3758. doi:10.1038/s41467-019-11674-z

44. Arnesen H, Hitch TCA, Steppeler C, et al. Naturalizing laboratory mice by housing in a farmyard-type habitat confers protection against colorectal carcinogenesis. *Gut Microbes*. 2021;13(1):1993581. doi:10.1080/19490976.2021.1993581

45. Jawhar S, Trawicka A, Jenneckens C, Bayer TA, Wirths O. Motor deficits, neuron loss, and reduced anxiety coinciding with axonal degeneration and intraneuronal Aβ aggregation in the 5XFAD mouse model of Alzheimer's disease. *Neurobiol Aging*. 2012;33(1):196.e29-196.e40. doi:10.1016/j.neurobiolaging.2010.05.027

46. Keren-Shaul H, Spinrad A, Weiner A, et al. A Unique Microglia Type Associated with Restricting Development of Alzheimer's Disease. *Cell*. 2017;169(7):1276-1290.e17. doi:10.1016/j.cell.2017.05.018

47. Liddelow SA, Guttenplan KA, Clarke LE, et al. Neurotoxic reactive astrocytes are induced by activated microglia. *Nature*. 2017;541(7638):481-487. doi:10.1038/nature21029

48. Habib N, Avraham-Davidi I, Basu A, et al. Massively parallel single-nucleus RNA-seq with DroNc-seq. *Nat Methods*. 2017;14(10):955-958. doi:10.1038/nmeth.4407

49. Saunders A, Macosko EZ, Wysoker A, et al. Molecular Diversity and Specializations among the Cells of the Adult Mouse Brain. *Cell*. 2018;174(4):1015-1030.e16. doi:10.1016/j.cell.2018.07.028

50. Zeisel A, Muñoz-Manchado AB, Codeluppi S, et al. Cell types in the mouse cortex and hippocampus revealed by single-cell RNA-seq. *Science*. 2015;347(6226):1138-1142. doi:10.1126/science.aaa1934

51. Batiuk MY, Martirosyan A, Wahis J, et al. Identification of region-specific astrocyte subtypes at single cell resolution. *Nat Commun*. 2020;11(1):1220. doi:10.1038/s41467-019-14198-8

52. Fumagalli L, Nazlie Mohebiany A, Premereur J, et al. Microglia heterogeneity, modeling and cell-state annotation in development and neurodegeneration. *Nat Neurosci*. 2025;28(7):1381-1392. doi:10.1038/s41593-025-01931-4

53. Paolicelli RC, Sierra A, Stevens B, et al. Microglia states and nomenclature: A field at its crossroads. *Neuron*. 2022;110(21):3458-3483. doi:10.1016/j.neuron.2022.10.020

54. Cheng YH, Ho MS. Disease-associated microglia in neurodegenerative diseases: Friend or foe? *PLOS Biol*. 2025;23(10):e3003426. doi:10.1371/journal.pbio.3003426

55. Berchtold NC, Coleman PD, Cribbs DH, Rogers J, Gillen DL, Cotman CW. Synaptic genes are extensively downregulated across multiple brain regions in normal human aging and Alzheimer's disease. *Neurobiol Aging*. 2013;34(6):1653-1661. doi:10.1016/j.neurobiolaging.2012.11.024

56. Srinivasan K, Friedman BA, Etxeberria A, et al. Alzheimer's Patient Microglia Exhibit Enhanced Aging and Unique Transcriptional Activation. *Cell Rep*. 2020;31(13). doi:10.1016/j.celrep.2020.107843

57. Yeh YW, Chaudhuri AS, Zhou L, Fang Y, Boysen P, Xiang Z. Mast Cells Are Identified in the Lung Parenchyma of Wild Mice, Which Can Be Recapitulated in Naturalized Laboratory Mice. *Front Immunol*. 2021;12. doi:10.3389/fimmu.2021.736692

58. Sanders AE, Arnesen H, Shepherd FK, et al. Comparison of mouse models of microbial experience reveals differences in microbial diversity and response to vaccination. Lakdawala S, ed. *mSphere*. 2024;9(2):e00654-23. doi:10.1128/msphere.00654-23

59. Zhu D, Huang M, Shen P, et al. TREM2 expression promotes liver and peritoneal M2 macrophage polarization in mice infected with Schistosoma japonicum. *J Cell Mol Med*. 2023;27(15):2261-2269. doi:10.1111/jcmm.17842

60. Katsuyama E, Humbel M, Suarez-Fueyo A, et al. CD38 in SLE CD4 T cells promotes Ca2+ flux and suppresses interleukin-2 production by enhancing the expression of GM2 on the surface membrane. *Nat Commun*. 2024;15(1):8304. doi:10.1038/s41467-024-52617-7

61. Erny D, Hrabě de Angelis AL, Jaitin D, et al. Host microbiota constantly control maturation and function of microglia in the CNS. *Nat Neurosci*. 2015;18(7):965-977. doi:10.1038/nn.4030

62. Ulland TK, Song WM, Huang SCC, et al. TREM2 Maintains Microglial Metabolic Fitness in Alzheimer's Disease. *Cell*. 2017;170(4):649-663.e13. doi:10.1016/j.cell.2017.07.023

63. Baik SH, Kang S, Lee W, et al. A Breakdown in Metabolic Reprogramming Causes Microglia Dysfunction in Alzheimer's Disease. *Cell Metab*. 2019;30(3):493-507.e6. doi:10.1016/j.cmet.2019.06.005

64. Condello C, Yuan P, Schain A, Grutzendler J. Microglia constitute a barrier that prevents neurotoxic protofibrillar Aβ42 hotspots around plaques. *Nat Commun*. 2015;6:6176. doi:10.1038/ncomms7176

65. Govindpani K, McNamara LG, Smith NR, et al. Vascular Dysfunction in Alzheimer's Disease: A Prelude to the Pathological Process or a Consequence of It? *J Clin Med*. 2019;8(5):651. doi:10.3390/jcm8050651

66. Li Q, Lebson L, Lee DC, et al. Chronological age impacts immunotherapy and monocyte uptake independent of amyloid load. *J Neuroimmune Pharmacol Off J Soc NeuroImmune Pharmacol*. 2012;7(1):202-214. doi:10.1007/s11481-011-9329-9

67. Hasselmann J, Blurton-Jones M. Human iPSC-derived microglia: A growing toolset to study the brain's innate immune cells. *Glia*. 2020;68(4):721-739. doi:10.1002/glia.23781

68. Schafer ST, Mansour AA, Schlachetzki JCM, et al. An in vivo neuroimmune organoid model to study human microglia phenotypes. *Cell*. 2023;186(10):2111-2126.e20. doi:10.1016/j.cell.2023.04.022

69. Canet G, Gratuze M, Zussy C, et al. Age-dependent impact of streptozotocin on metabolic endpoints and Alzheimer's disease pathologies in 3xTg-AD mice. *Neurobiol Dis*. 2024;198:106526. doi:10.1016/j.nbd.2024.106526

70. Zare Jousheghani Z, Singh NP, Patro R. Oarfish: enhanced probabilistic modeling leads to improved accuracy in long read transcriptome quantification. *Bioinformatics*. 2025;41(Supplement_1):i304-i313. doi:10.1093/bioinformatics/btaf240

71. Love MI, Huber W, Anders S. Moderated estimation of fold change and dispersion for RNA-seq data with DESeq2. *Genome Biol*. 2014;15(12):550. doi:10.1186/s13059-014-0550-8

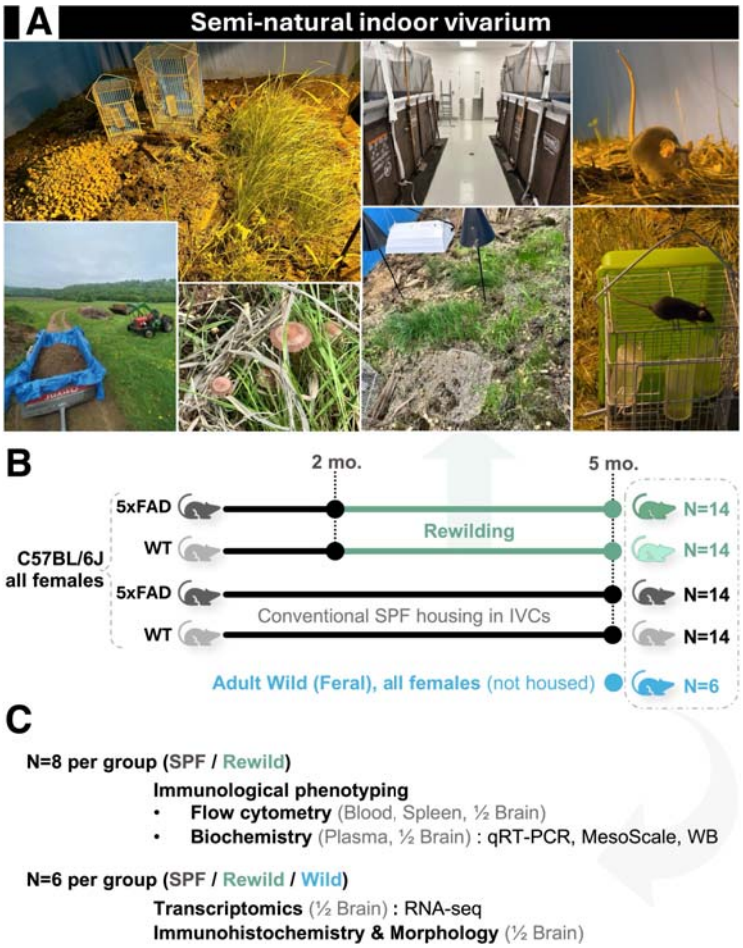

Figure 1. Experimental design, housing conditions, and cohort allocation across assays. **(A)** Representative photographs of the semi-natural indoor vivarium used for the rewilding exposure. A detailed description of the vivarium platform (structure, substrates, enrichment elements, and environmental features) was reported previously [37]. **(B)** Two-month-old female SPF 5xFAD mice and their age-matched female WT littermates (SPF-WT) mice underwent routine health assessment and baseline body-weight measurement, then were randomly assigned to standard SPF housing in individually ventilated cages (IVCs) or rewilding housing in the indoor vivarium (N=14 per group): WT-SPF, WT-Rewild, 5xFAD-SPF, and 5xFAD-Rewild. WT and 5xFAD mice were housed in two separate, strictly identical vivariums located side-by-side in the same room to avoid mixing of visually indistinguishable mice on the same C57BL/6J background. Rewilding was conducted for 3 months (2 to 5 months of age). At study endpoint, rewilded mice were captured using Havahart-type live traps and processed for downstream assays. **(C)** For immunophenotyping and biochemistry, N=8 per group (SPF vs Rewild) were used for flow cytometry (blood, spleen, and right brain hemisphere) and biochemical assays (plasma and left brain hemisphere; qRT-PCR, Meso Scale Discovery (MSD) multiplex immunoassays, and immunoblotting). For transcriptomics and histology, N=6 per group were used for brain RNA

sequencing (left hemisphere) and immunohistochemistry/morphology (right hemisphere, fixed). An additional group of adult Wild (Feral) female mice (N=6), captured outdoors and euthanized immediately (not housed under SPF or rewilding conditions), was included only for brain transcriptomic profiling (RNA-seq). Flow cytometry data are shown in **Figures 2-7**, biochemical analyses in **Figures 7-8,10**, immunohistochemistry/morphology in **Figure 8**, and transcriptomic analyses in **Figures 9-11**.

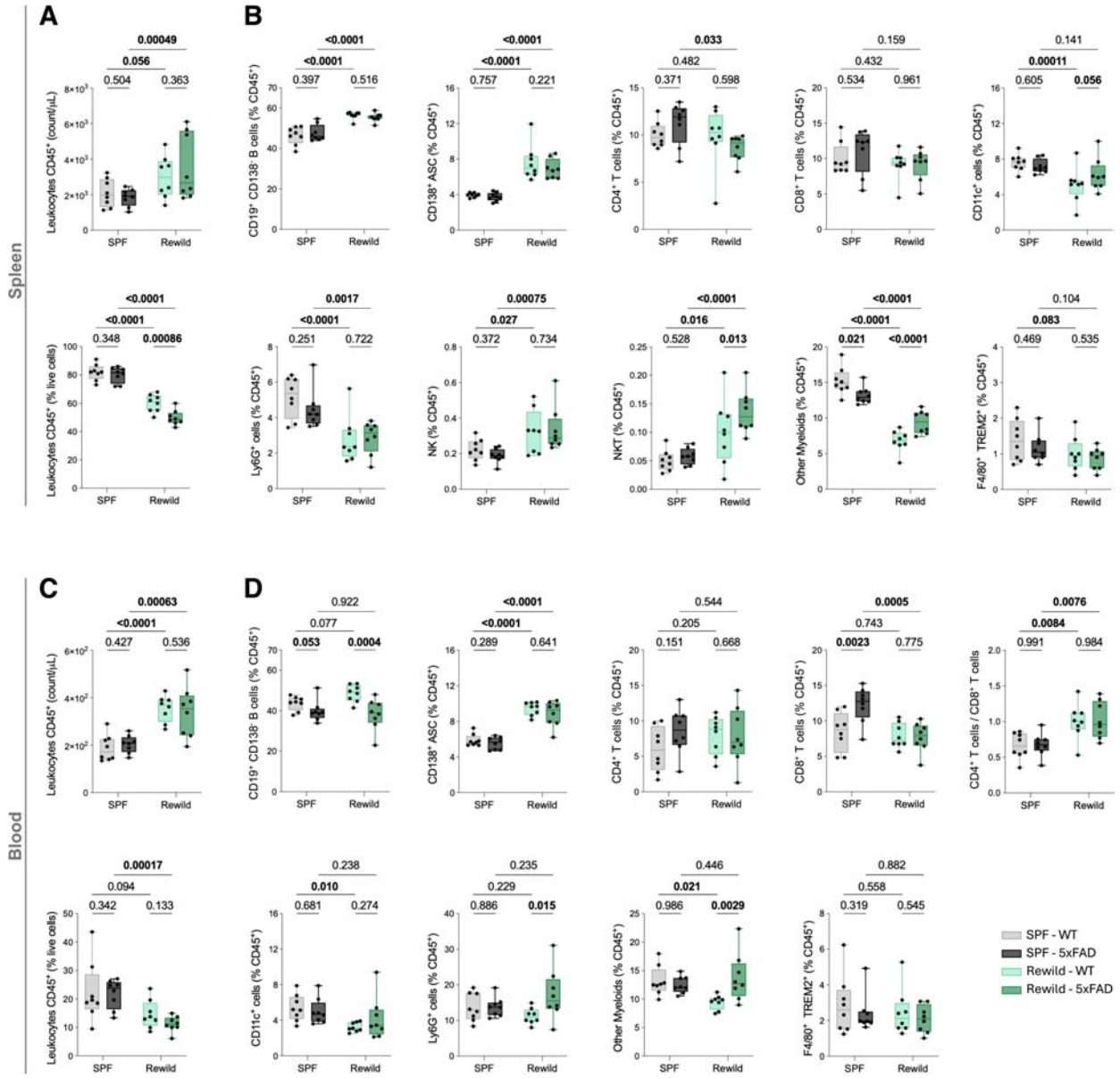

Figure 2. Rewilding reshapes systemic leukocyte composition in spleen and blood. Flow cytometry quantification of leukocytes in spleen **(A-B)** and blood **(C-D)** from female mice housed under SPF conditions or in the indoor vivarium (Rewild): SPF-WT, SPF-5xFAD, Rewild-WT, and Rewild-5xFAD (N = 8 per group). Gating strategies are provided in **Supplementary Figure 1**. **(A, C)** Total leukocytes are shown as absolute abundance (volumetric counts; $CD45^+$ events per µL of acquired sample; acquisition target ~100µL per sample) and as frequency ($CD45^+$, % of live cells). **(B, D)** Frequencies of major leukocyte subsets are expressed as % of $CD45^+$. In spleen, subsets include $CD138^-CD19^+$ B cells, $CD138^+$ antibody-secreting cells (ASCs), $CD4^+$ T cells, $CD8^+$ Tcells, NK, NKT, $Ly6G^+$ cells, $CD11c^+$ cells, $F4/80^+TREM2^+$ macrophages, and other myeloids (including macrophage and monocyte populations). In blood, only subsets detectable in circulation are shown, and the T4/T8 ratio is included. Data are plotted as individual values overlaid on box-and-whisker plots (box: 25th-75th percentile; center line: median; whiskers: min-max). Statistical

analyses were performed in R, as described in Methods. Abundances for leukocyte subsets (counts/µL) are provided in **Supplementary Figure 2**.

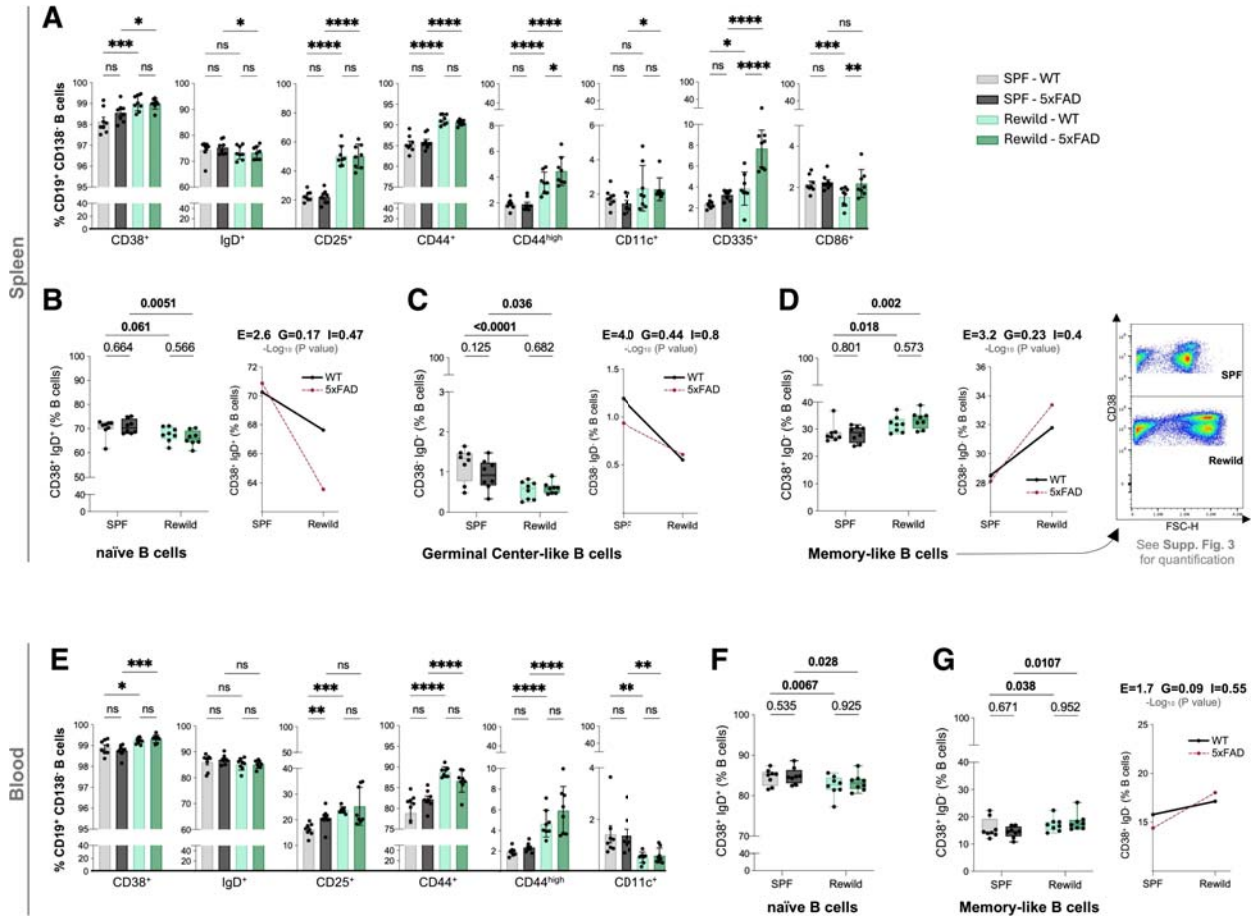

Figure 3. Rewilding modulates B-cell phenotypes and CD38/IgD-defined B-cell subset composition in spleen and blood. Flow cytometry analysis of B-cell phenotypes in spleen **(A-D)** and blood **(E-G)** from female SPF-WT, SPF-5xFAD, Rewild-WT, and Rewild-5xFAD mice (N = 8 per group). Gating strategies are provided in **Supplementary Figure 1**. **(A, E)** Frequencies of marker-positive cells within B lymphocytes are shown for the indicated markers. In spleen **(A)**: CD38, IgD, CD25, CD44, CD44^{high}, CD11c, CD335 (NKp46), and CD86. In blood **(E)**: CD38, IgD, CD25, CD44, CD44^{high}, and CD11c. Values are expressed as % of total B lymphocytes. **(B-D)** Splenic B-cell subset frequencies expressed as % of B lymphocytes, using an operational CD38/IgD definition: naïve B cells (CD38^{+}IgD^{+}) **(B)**, germinal center-like B cells (CD38^{-}IgD^{-}) **(C)**, and memory-like B cells (CD38^{+}IgD^{-}) **(D)**. The right panel in **(D)** shows representative CD38 versus FSC plots (SPF vs Rewild) illustrating cell population heterogeneity within the CD38^{+}IgD^{-} (memory-like) gate; corresponding quantification of these fractions is provided in **Supplementary Figure 3**. **(F, G)** Circulating B-cell subset frequencies expressed as % of B lymphocytes: naïve B cells (CD38^{+}IgD^{+}) **(F)** and memory-like B cells (CD38^{+}IgD^{-}) **(G)**. For the boxplot panels **(A-G)**, statistical analyses were performed in R using the same pipeline as described in Methods. The adjacent interaction plots (where shown) were generated independently using a two-way ANOVA

full model; E, G, and I denote $-\log_{10}(P)$ for the main effects of Environment, Genotype, and their Interaction, respectively. *$p < 0.05$, **$p < 0.01$, ***$p < 0.001$, ****$p < 0.0001$; ns: not significant.

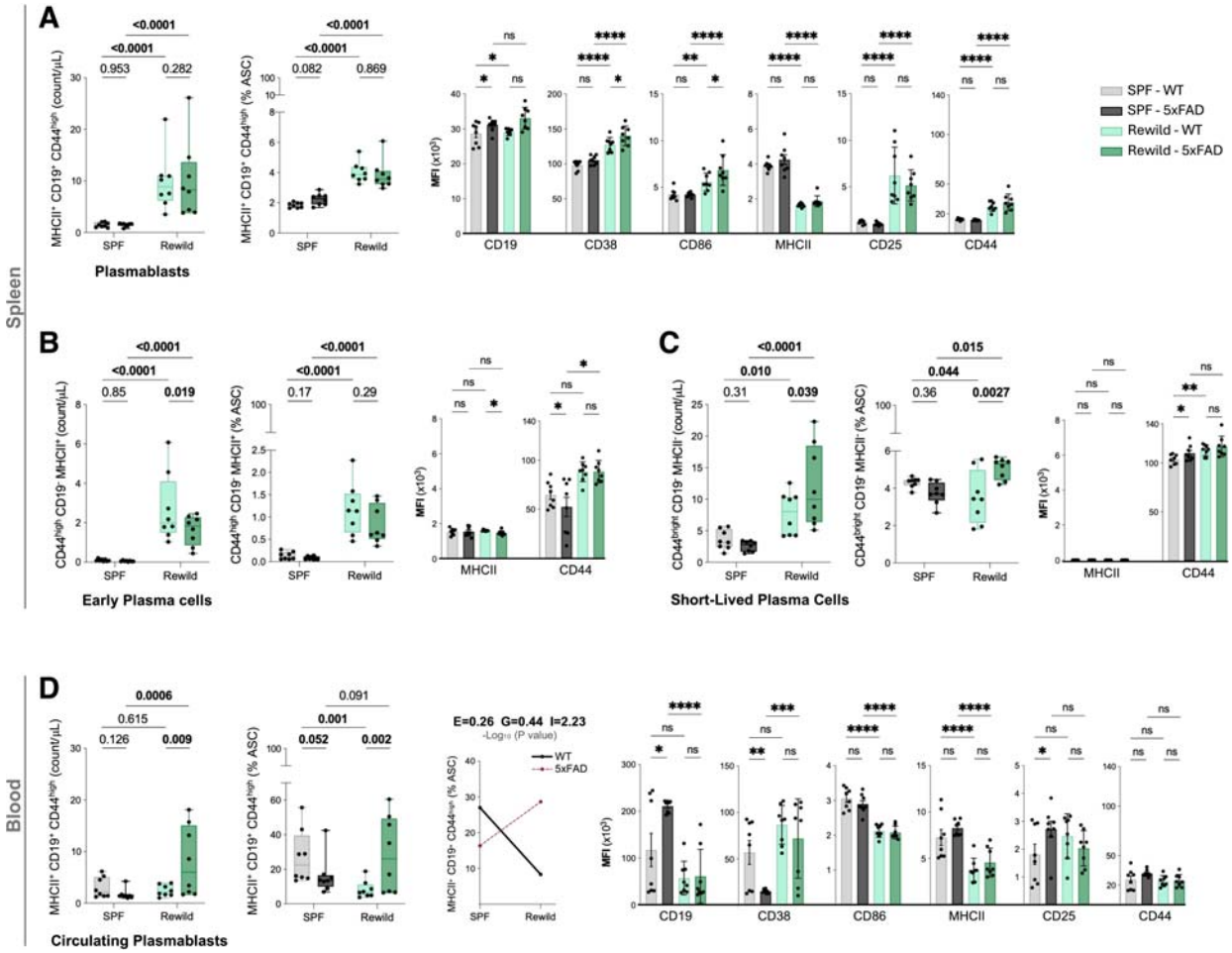

Figure 4. Rewilding expands ASC subsets and accelerates maturation in spleen and blood. Flow cytometry analysis of splenic plasmablasts and plasma cells **(A-C)** and circulating plasmablasts **(D)** from female SPF-WT, SPF-5xFAD, Rewild-WT, and Rewild-5xFAD mice (N = 8 per group). Gating strategy of ASCs subsets is shown in **Supplementary Figure 1**. **(A, D)** Plasmablasts are shown as absolute abundance (counts/µL of acquired sample) and as frequency (% of antibody-secreting cells) in spleen **(A)** and blood **(D)**. **(B, C)** Early plasma cells and short-lived plasma cells are shown as absolute abundance, and as frequency of ASCs in spleen. The interaction plot in **(D)** summarizes the full two-way ANOVA model with E, G, and I denoting -$\log_{10}$(P) for the main effects of Environment, Genotype, and their Interaction, respectively. Expression of the indicated markers on ASCs subsets are shown as MFI in spleen **(A-C)** and blood **(D)**: CD19, CD38, CD86, MHCII, CD25, and CD44. Statistical testing, transformations, and outlier handling were performed using the same pipeline described in Methods. *$p < 0.05$, **$p < 0.01$, ***$p < 0.001$, ****$p < 0.0001$; ns: not significant.

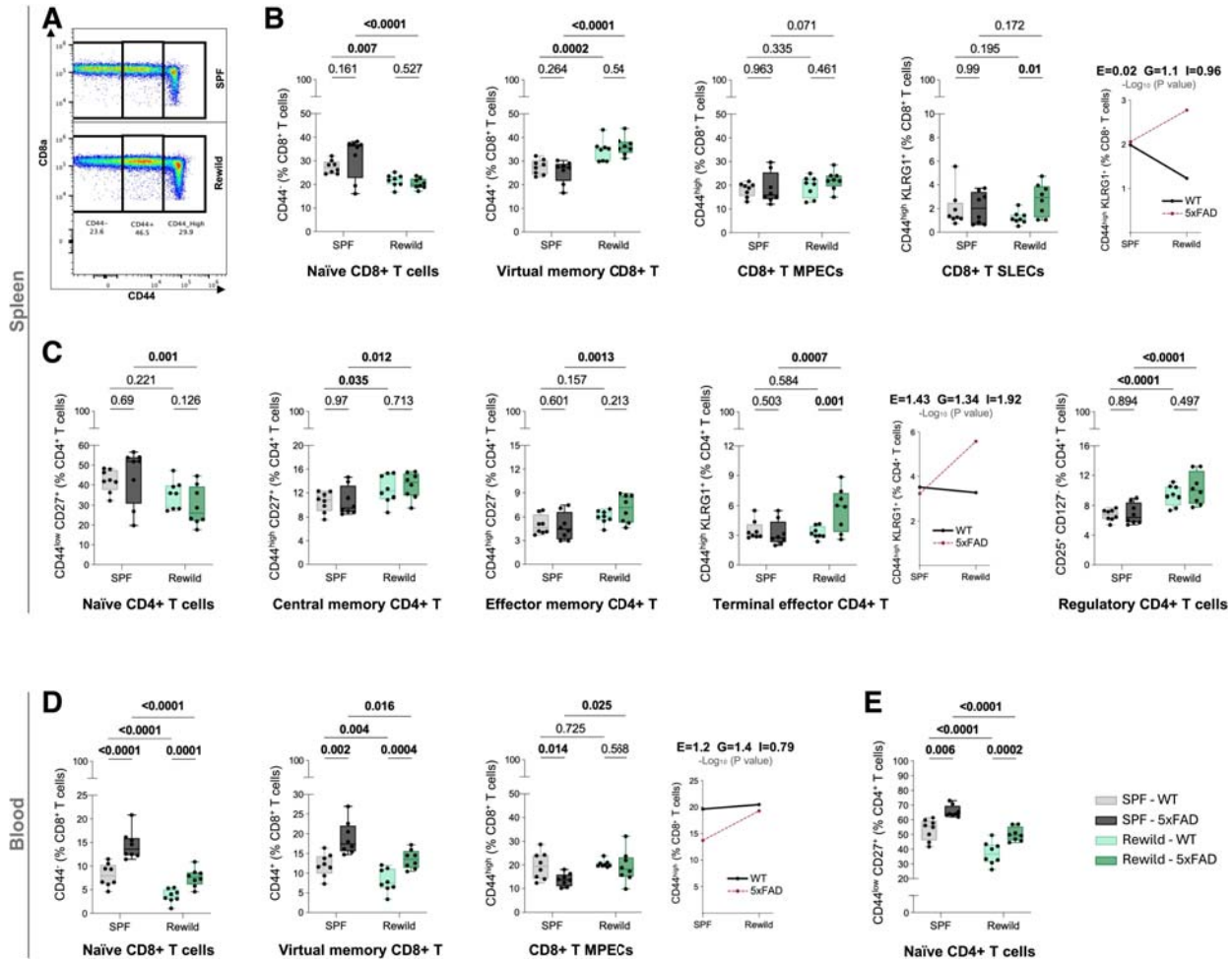

Figure 5. Rewilding shifts circulating and splenic T-cell differentiation states. Flow cytometry analysis of T-cell subsets in spleen **(A-C)** and blood **(D-E)** from female SPF-WT, SPF-5xFAD, Rewild-WT, and Rewild-5xFAD mice (N = 8 per group). Gating strategies for subset definitions are provided in **Supplementary Figure 1**. **(A)** Representative CD8a versus CD44 plots illustrating the gating of splenic $CD8^+$ T-cell subsets and highlighting a global shift toward higher CD44 expression in rewilded mice relative to SPF controls. **(B)** Splenic $CD8^+$ T-cell subset frequencies (% of $CD8^+$ T cells): naïve $CD8^+$ T-cell, virtual memory $CD8^+$ T-cell, memory precursor effector cells ($CD8^+$ MPECs), and short-lived effector cells ($CD8^+$ SLECs). **(C)** Splenic $CD4^+$ T-cell subset frequencies (% of $CD4^+$ T cells): naïve $CD4^+$ T-cell, central memory $CD4^+$ T-cell, effector memory $CD4^+$ T-cell, terminal effector $CD4^+$ T-cell, and regulatory $CD4^+$ T-cells. **(D)** Blood $CD8^+$ T-cell subset frequencies (% of $CD8^+$ T cells): naïve $CD8^+$ T-cell, virtual memory $CD8^+$ T-cell, and $CD8^+$ MPECs. **(E)** Blood naïve $CD4^+$ T cells shown as % of $CD4^+$ T cells (other $CD4^+$ differentiation subsets were too sparse for robust quantification in blood). Interaction plots (where shown) and statistical testing were performed as described in Methods.

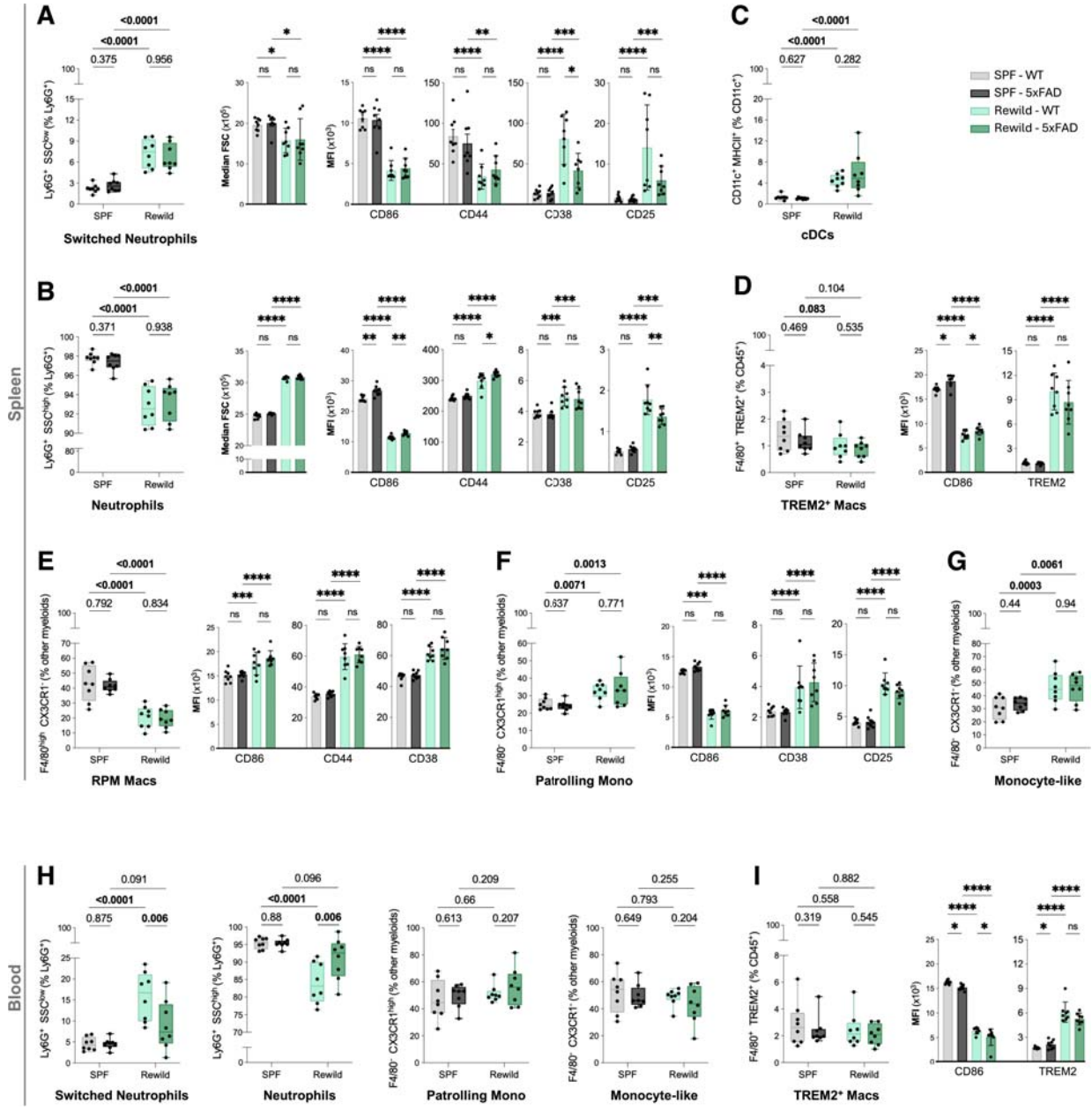

Figure 6. Rewilding remodels myeloid phenotypes and activation-marker expression in spleen and blood. Flow cytometry analysis of myeloid subsets in spleen **(A-G)** and blood **(H-I)** from female SPF-WT, SPF-5xFAD, Rewild-WT, and Rewild-5xFAD mice (N = 8 per group). Gating strategies are provided in **Supplementary Figure 1**. **(A**) Switched neutrophils in spleen, quantified as $Ly6G^{+}SSC^{low}$ (% of $Ly6G^{+}$), and **(B)** Splenic neutrophils quantified as $Ly6G^{+}SSC^{high}$ (% of $Ly6G^{+}$), along with their median-FSC and marker expression (MFI) for CD86, CD44, CD38, and CD25. **(C)** Splenic conventional dendritic cells (cDCs) quantified as $CD11c^{+}MHCII^{+}$ (% of $CD11c^{+}$). **(D)** Splenic $TREM2^{+}$ macrophages quantified as $F4/80^{+}TREM2^{+}$ (% of $CD45^{+}$), with marker expression (MFI) for CD86 and TREM2. **(E)** Splenic red pulp macrophages (RPM Macs) quantified as $F4/80^{high}CX3CR1^{-}$ (% of other myeloids), with marker expression (MFI) for CD86, CD44, and CD38. **(F)** Splenic patrolling monocytes quantified as $F4/80^{-}CX3CR1^{high}$ (% of other

myeloids), with marker expression (MFI) for CD86, CD38, and CD25. **(G)** Splenic monocyte-like cells quantified as F4/80^{-}CX3CR1^{-} (% of other myeloids). **(H)** Blood myeloid subsets: switched neutrophils, neutrophils, patrolling monocytes and monocyte-like cells. **(I)** Blood TREM2^{+} macrophages quantified as F4/80^{+}TREM2^{+} (% of CD45^{+}), with marker expression (MFI) for CD86 and TREM2. Statistical testing, transformations, and outlier handling were performed as described in Methods. *$p < 0.05$, **$p < 0.01$, ***$p < 0.001$, ****$p < 0.0001$; ns: not significant.

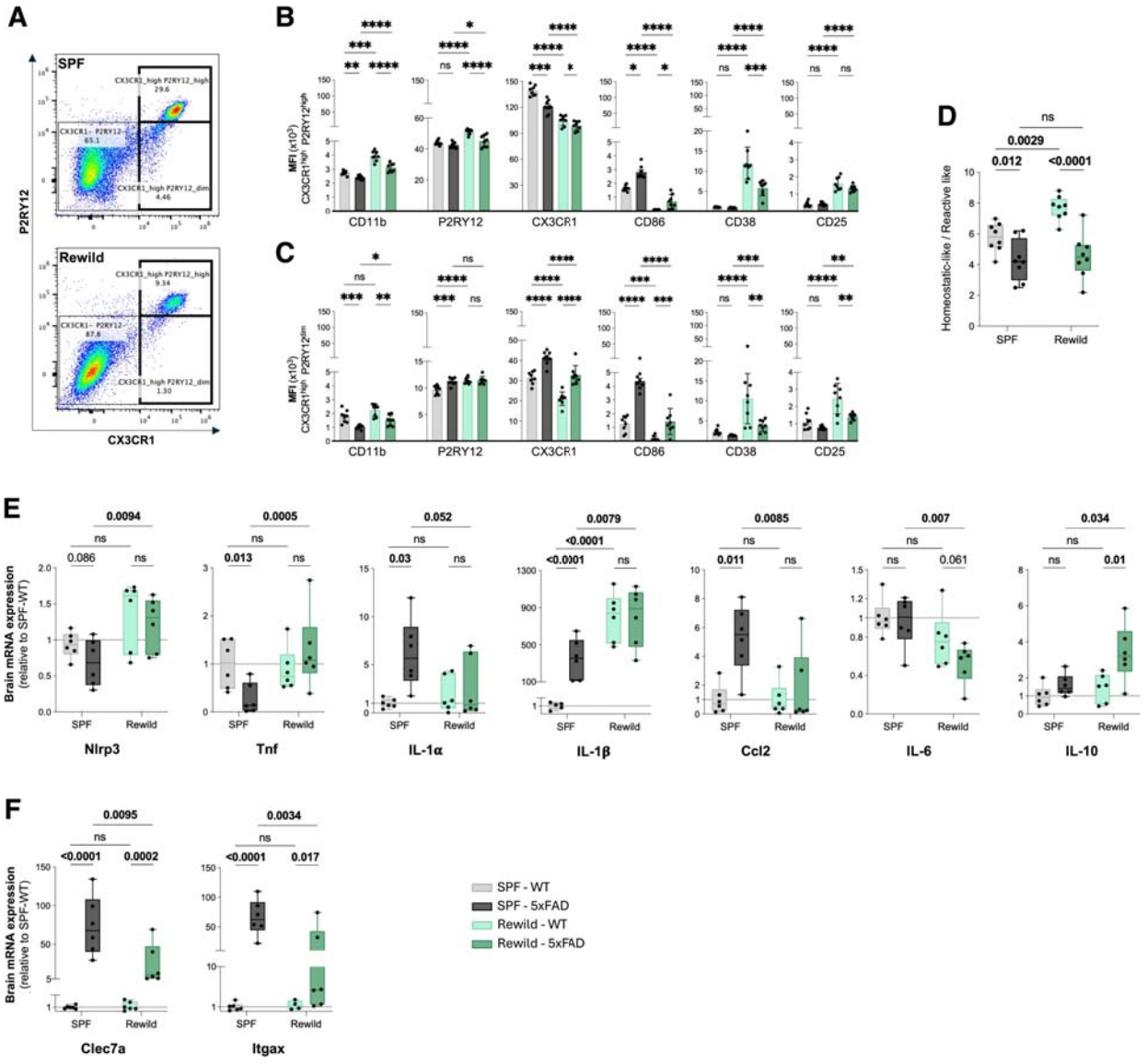

Figure 7. Rewilding modifies microglial marker expression and inflammatory gene programs in the brain. Flow cytometry and qRT-PCR analyses were performed on brain tissue from female SPF-WT, SPF-5xFAD, Rewild-WT, and Rewild-5xFAD mice (N = 8 per group). The brain flow cytometry gating strategy is shown in **Supplementary Figure 5**. **(A)** Representative bivariate plots (P2RY12 vs CX3CR1) illustrating the microglial gating approach under SPF and Rewild conditions and the distribution of CX3CR1/P2RY12-defined subsets. **(B)** Microglial marker expression (MFI) for CD11b, P2RY12, CX3CR1, CD86, CD38, and CD25 in $CX3CR1^{high}P2RY12^{high}$ cells (homeostatic-like microglia). **(C)** The same markers in $CX3CR1^{high}P2RY12^{dim}$ cells (reactive-like microglia). **(D)** Homeostatic-like/Reactive-like ratio, calculated as $(CX3CR1^{high}P2RY12^{high})/(CX3CR1^{high}P2RY12^{dim})$ based on event counts within each sample. This ratio-based metric was used to minimize sensitivity to between-sample variation in total brain immune cell yield introduced during tissue dissociation and processing. **(E-F)** Brain mRNA expression measured by qRT-PCR for Nlrp3, Tnf, IL-1α, IL-1β, Ccl2, IL-6, and IL-10 **(E)**,

and for Clec7a, Itgax **(F)**, normalized to housekeeping gene Gapdh. Data are displayed as fold change relative to the SPF-WT group. Statistical testing was performed on $\log_2$-transformed fold-change values using a two-way ANOVA model with Šidák's correction. MFI values were analyzed as described in Methods. *$p < 0.05$, **$p < 0.01$, ***$p < 0.001$, ****$p < 0.0001$; ns: not significant.

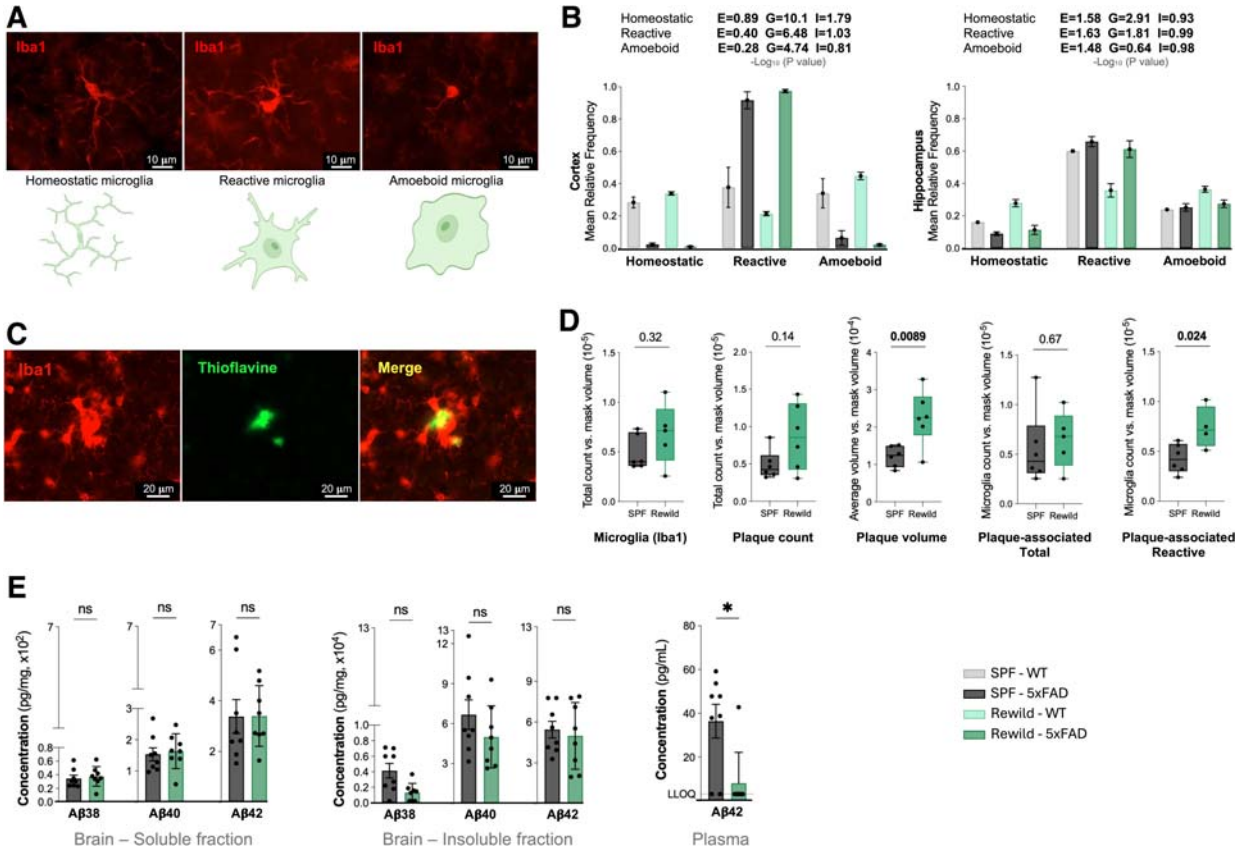

Figure 8. Rewilding modulates microglia–Aβ interactions and Aβ burden in 5xFAD brain. Histological and biochemical analyses were performed in female SPF-WT, SPF-5xFAD, Rewild-WT, and Rewild-5xFAD mice (N = 6-8 per group, as indicated). Microglia were visualized by Iba1 immunostaining and amyloid plaques by Thioflavin S staining. **(A)** Representative Iba1 images illustrating microglial morphological states used for classification: Homeostatic (State 0), Reactive (State 1), and Amoeboid (State 2). Scale bar, 10 µm. **(B)** Quantification of microglial morphological states shown as mean cell frequency in cortex and hippocampus (right hemisphere fixed; N = 6 per group). Insets report -log10(P) for the main effects of Environment (E) and Genotype (G) and their Interaction (I) from the full two-factor ANOVA model, as indicated in Methods. **(C)** Representative images showing microglia and amyloid plaques with Iba1 (microglia), Thioflavin S (plaques), and merged channels. Scale bar, 20µm. **(D)** Quantification of total microglial signal (Iba1), plaque count, plaque volume, and plaque-associated microglial measures, total and reactive, as indicated. (right hemisphere fixed; N = 6 per group). **(E)** Human Aβ peptide quantification by MSD immunoassays in brain and plasma (N = 8 per group). Brain concentrations are expressed as pg per mg of total proteins; plasma $A\beta_{42}$ is reported in pg/mL. Statistical testing was performed on $\log_{10}$-transformed data. Values below the lower limit of quantitation (LLOQ) are indicated where applicable. Plasma $A\beta_{40}$ was bellow detection range for all samples (not shown). Two-group comparisons used two-tailed t-tests or Mann-Whitney tests as

appropriate. Exact p-values and significance annotations are shown on the plots (*$p < 0.05$; ns, not significant).

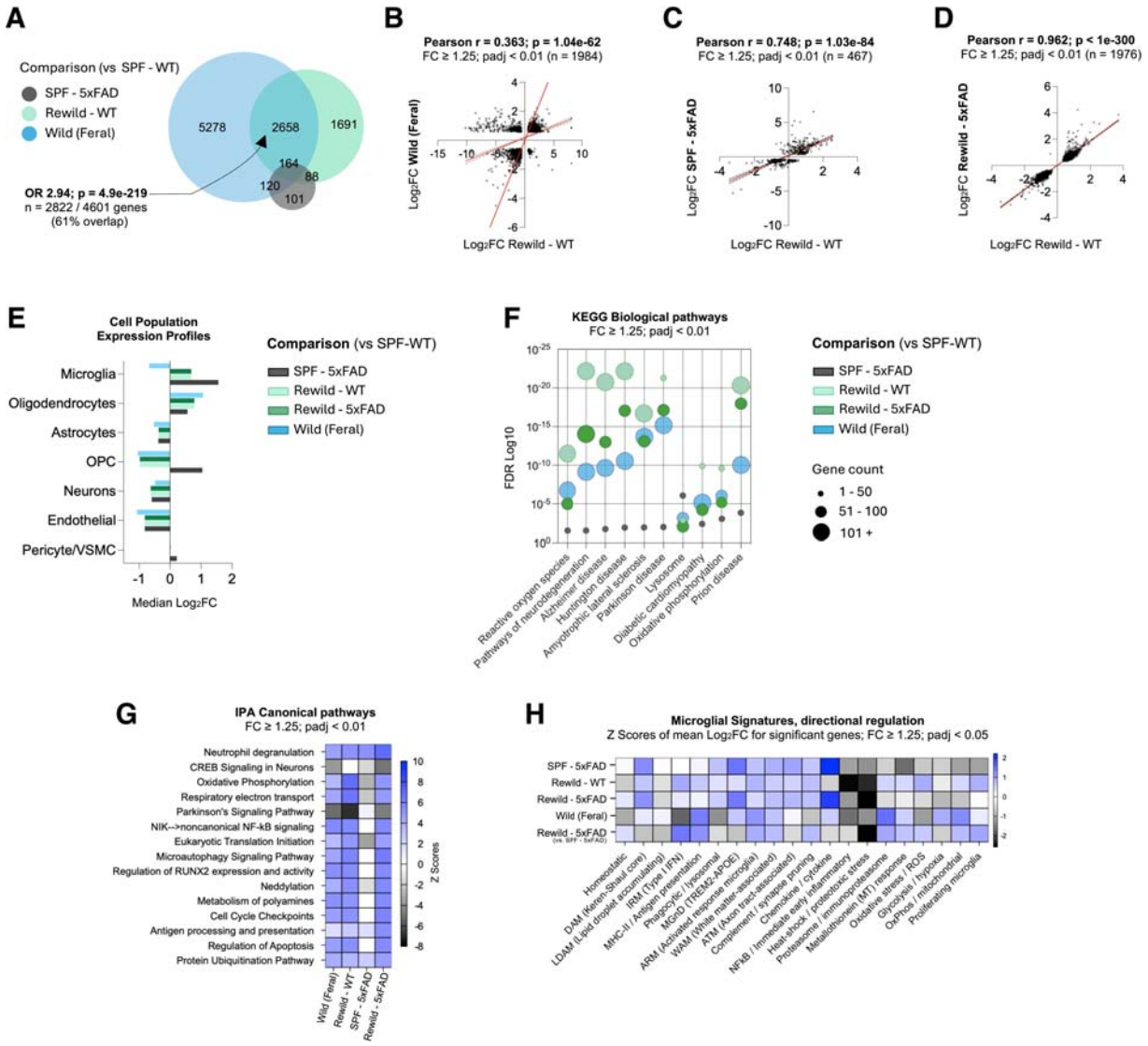

Figure 9. Rewilding substantially redirects brain transcriptional signatures. Bulk RNA sequencing was performed on left brain hemispheres from female mice (N = 6 per group): SPF-WT, SPF-5xFAD, Rewild-WT, Rewild-5xFAD, and Wild (Feral). Differential expression was assessed using DESeq2. Unless indicated, significance thresholds are FC ≥ 1.25 ($|\log_2 FC| \geq \sim 0.32$) and padj < 0.01. **(A)** Venn diagram showing overlap of significantly regulated genes across comparisons vs SPF-WT for SPF-5xFAD, Rewild-WT, and Wild (Feral). The number of significant genes in each comparison and overlap sizes are shown. Statistics for the largest overlap are reported. **(B-D)** Pearson correlation of $\log_2 FC$ values among shared significant genes (FC ≥ 1.25; padj < 0.01), comparing Rewild-WT with Wild (Feral) **(B)**, SPF-5xFAD **(C)**, and Rewild-5xFAD **(D)**. Sample sizes (n), Pearson r, and p-values are indicated in each panel. **(E)** Cell population expression profiles summarizing the median $\log_2 FC$ of significant genes across comparisons versus SPF-WT for major brain cell populations (Microglia, Oligodendrocytes, Astrocytes, OPC, Neurons, Endothelial, Pericyte/Vascular Smooth Muscle Cells). Bar shading

indicates comparison group. **(F)** Bubble plot of enriched KEGG biological pathways across comparisons (FC ≥ 1.25; padj < 0.01). Bubble color indicates the comparison group, and the y-axis shows enrichment significance (FDR $\log_{10}$). Dot size encodes the number of significant genes (1–50, 51–100, or ≥101) contributing to each pathway. **(G)** Heatmap of IPA canonical pathways across comparisons (FC ≥ 1.25; padj < 0.01), displayed as IPA activation Z-scores. **(H)** Directional regulation of curated microglial gene signatures across mouse contrasts, shown as Z-scores of mean log2FC for significant genes, showing coordinated shifts in DAM, phagocytic/lysosomal, antigen-presentation, and metabolic programs in rewilded 5xFAD mice.

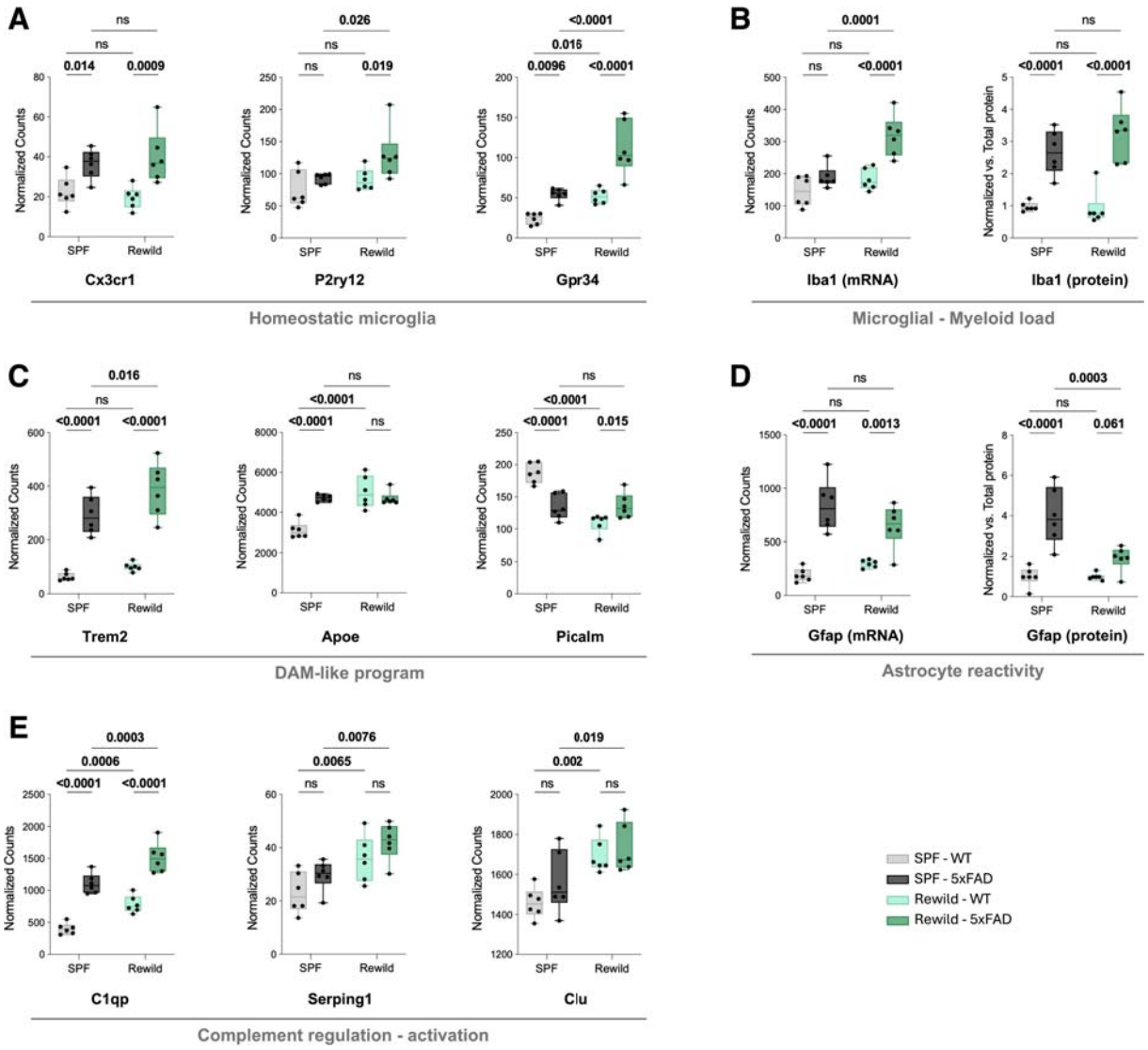

Figure 10. Rewilding modulates microglial and AD-associated gene signatures in the brain. Bulk RNA-seq and immunoblot analyses were performed on brain tissue from female SPF-WT, SPF-5xFAD, Rewild-WT, and Rewild-5xFAD mice (N = 6 per group). For RNA-seq panels, expression is shown as DESeq2-normalized counts. For immunoblots, ECL signal intensities were normalized to total protein (Ponceau staining). **(A)** Homeostatic microglial gene expression: Cx3cr1, P2ry12, and Gpr34. **(B)** Microglial/myeloid load assessed by RNA-seq Aif1 expression and Iba1 protein levels (immunoblot). **(C)** Microglial activation/DAM-like genes: Trem2, Apoe, and Picalm. **(D)** Astrocyte reactivity assessed by RNA-seq Gfap expression and GFAP protein levels (immunoblot). **(E)** Complement-related genes: C1qp, Serping1, and Clu. For RNA-seq panels, p-values were derived from DESeq2 model contrasts. For immunoblot quantification, group comparisons were performed using a two-way repeated measures ANOVA with Šidák's multiple comparison test.

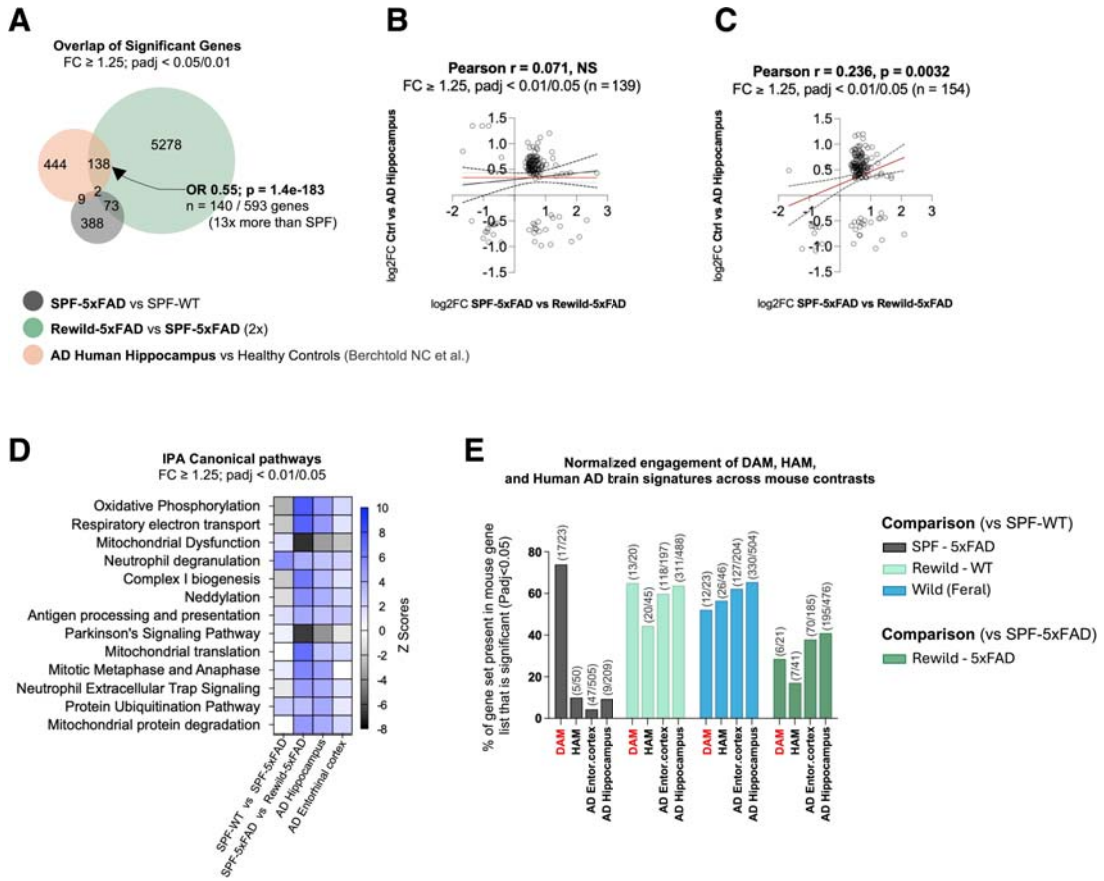

Figure 11. Rewilding enhances transcriptional convergence between 5xFAD mouse brains and human Alzheimer's disease. (A) Overlap of differentially expressed genes (DEGs) between Rewild-5xFAD vs SPF-5xFAD (two-fold contrast) and human AD hippocampus (Berchtold Nat Commun). Rewilded 5xFAD mice show a markedly larger overlap (140 shared DEGs; OR = 0.55, $p = 1.4 \times 10^{-183}$) representing a 13-fold increase compared with the overlap observed under SPF conditions (SPF-5xFAD vs SPF-WT). **(B)** Cross-species comparison of $\log_2$ fold changes between SPF-5xFAD and human AD hippocampus, showing no meaningful correlation with human AD hippocampus (Pearson r = 0.071, NS; n = 139 DEGs), highlighting the weak translational relevance of conventional SPF housing. **(C)** A significant correlation is observed (Pearson r = 0.236, p = 0.0032; n = 154 DEGs) between rewilded 5xFAD mice and the human AD hippocampus. **(D)** Canonical pathway analysis (IPA) of DEGs from SPF-5xFAD, Rewild-5xFAD (2x), and two human AD regions (hippocampus and entorhinal cortex). Rewilding amplifies the enrichment of pathways strongly implicated in human AD, including Oxidative Phosphorylation, Respiratory Electron Transport, Mitochondrial Dysfunction, Complex I biogenesis, Protein Ubiquitination, Neutrophil Degranulation/NETs, and Antigen Processing and Presentation, bringing the mouse transcriptional signature closer to human disease. Z-scores reflect pathway directionality across species. **(E)** Normalized engagement of DAM, HAM, and human AD brain transcriptional

signatures across mouse contrasts, expressed as the percentage of signature genes significantly regulated, showing increased overlap with human AD signatures in rewilded mice.